

Dynamics of Taylor bubble interface in vertical turbulent counter-current flow

Jan Kren^{a,b}, Boštjan Zajec^a, Iztok Tiselj^{a,b,*}, Samir El Shawish^a, Žiga Perne^a, Matej Tekavčič^a, Blaž Mikuz^{a,*}

^a Reactor Engineering Division, Jožef Stefan Institute, Jamova 39 Ljubljana, Slovenia

^b Faculty of Mathematics and Physics, University of Ljubljana, Jadranska 19, Ljubljana, Slovenia

ARTICLE INFO

Keywords:
Slug flow
Taylor bubble
Interfacial waves

ABSTRACT

Dynamics of the Taylor bubble interface in the vertical counter-current flow was analyzed with video recordings at 100 – 800 frames per second. Taylor bubbles in air-water mixture were studied on time intervals of up to several minutes in stagnant conditions, where buoyancy is dynamically balanced by the inertial bubble drag in the downward turbulent flow. Taylor bubbles of length from 4 to 10 cm were observed in a pipe of 26 mm diameter at Reynolds numbers based on liquid superficial velocity around 6000. Algorithms, developed for analysis of the interface from the video frames were dedicated to the analysis of the cap and the body of the Taylor bubble. The long time averaging of up to 10 min samples do not end up with axisymmetric time-averaged shape of the bubble, but with an asymmetric bullet-train shape, with the thinnest liquid film observed on the belly of the bullet-train shape bubble. The main result of this study is based on high relative sensitivity of our measurements, which was sufficient to track the dynamics of the tiny disturbance waves with a tenth of mm amplitudes traveling along the interface of the Taylor bubble. Cross-correlations of time-dependent interface fluctuations measured at different spatial positions allowed us to measure propagation speeds of the interface waves. When averaged over sufficiently long time intervals of around a minute, the time averaged propagation velocities are shown to be equal to the convective velocity of the interface. Moreover, waves propagating on both sides of the two-dimensional photographs show clear correlation; crest of the wave on one side of the bubble photograph corresponds to the trough of the wave on the other side.

1. Introduction

Flows of gas-liquid mixtures in a pipe may exhibit a variety of two-phase flow patterns. A basic classification divides multiphase flows in vertical pipes into bubbly, slug, churn, annular or misty flow regimes (Wallis, 1969). A particular pattern that one observes depends on the flow velocities of both phases, volume fractions of the phases, the material properties of the fluids and the pipe size and orientation. Our focus in this study is Taylor bubble flow, which is a sub-pattern of the slug flow. Taylor bubble is a bullet-shaped bubble, which is moving in a vertical pipe and occupies almost the entire cross-section of the pipe. Slug flows with Taylor bubbles are present in numerous practical applications, from vaporizers, boilers, filtration and membrane processes (Morgado et al., 2016), to extreme events in the petroleum industry (Zhou and Prosperetti 2019), or steam generators in nuclear power plants.

Taylor bubble motion is determined by the magnitudes of inertial, viscous, gravitational and interfacial forces. The most frequently used dimensionless numbers are:

- $Eo = g(\rho_L - \rho_G)D^2/\sigma$; Eotvos number as the ratio of gravitational effects and surface tension.
- $Mo = g\mu_L^4(\rho_L - \rho_G)/\rho_L^2\sigma^3$; Morton number contains the properties of the fluid including viscosity
- $Fr = U_0/\sqrt{gD(\rho_L - \rho_G)/\rho_L}$; Froude number as the ratio of inertial and gravitational forces.

Other dimensionless numbers can be derived from Eo , Mo and Fr and include Archimedes number $Ar = (Eo^3/Mo)^{1/2}$, Weber number $We = Eo Fr^2$, inverse viscosity $N_f = Ar^{1/2}$, and various Reynolds numbers based on the speed of the liquid $Re_L = U_L N_f$ or bubble $Re_{TB} = U_0 N_f$.

* Corresponding authors.

E-mail addresses: iztok.tiselj@ijs.si (I. Tiselj), blaz.mikuz@ijs.si (B. Mikuz).

<https://doi.org/10.1016/j.ijmultiphaseflow.2023.104482>

Received 23 December 2022; Received in revised form 7 March 2023; Accepted 11 April 2023

Available online 12 April 2023

0301-9322/© 2023 The Author(s). Published by Elsevier Ltd. This is an open access article under the CC BY-NC-ND license (<http://creativecommons.org/licenses/by-nc-nd/4.0/>).

Our experiments are performed in the so-called inertia dominant region, where viscosity ($N_f \approx 10^4$) and surface tension ($Eu \approx 100$) effects are weak (Wallis, 1969) and the Taylor bubble drift velocity is given by Davies and Taylor (1950) as:

$$U_0 = k\sqrt{gD}, \quad (1)$$

where $k \approx Fr$ for low ρ_G/ρ_L ratio. The correlation (1) predicts U_0 for Taylor bubbles in our 26 mm diameter pipe between 0.167 m/s and 0.192 m/s for the values of the constant $k=0.33$ and 0.38 , respectively, proposed by different sources and collected by Liberzon et al. (2006). This is close to the average measured liquid velocity U_L in our experiments between -0.16 m/s and -0.19 m/s, which flows in the downward direction (minus sign) and keeps the bubble at fixed position. Relation proposed by Nicklin et al. (1962) connects terminal velocity of the bubble U_t with a given liquid velocity U_L

$$U_t = C U_L + U_0. \quad (2)$$

Polonsky et al. (1999a, 1999b) proposed $C \approx 1.2$ for turbulent flows of liquid ahead of the bubble. In our experiment, the terminal velocity of the bubble $U_t = 0$ was achieved at liquid velocity around $U_L = -0.18$ m/s. This is slightly higher than the one predicted by Eq. (2): $U_t = -U_0/C = -0.14$ m/s, which suggests that the value $C \approx 1.2$ is not accurate for counter-current flow regime. However, measurements of Polonsky et al. were performed only at positive (upward) terminal velocities of the bubble, where the bubble retains axisymmetric shape (Dumitrescu 1943) and have shown that soon after the liquid flow was directed downward the Taylor bubble became unstable. One of the first experiments in the counter-current turbulent flow were performed by Martin (1976), where the air-water mixtures were investigated in circular pipes of diameter $D = 2.6, 10.16$ and 14.0 cm. He demonstrated that the bubble velocity in the counter-current slug flow could not be adequately represented by the existing theories for co-current background flow or stagnant liquid. This is due to the bubble instability, which increases the bubble velocity when the bubble is pushed from the axis of the pipe. Lu and Prosperetti (2006) have performed analytical stability analysis and have shown that breakup of Taylor bubble symmetry happens at liquid velocities below critical negative velocity of $U_c = -0.13\sqrt{gD}$. Numerical analysis of symmetry breakup was performed by Figueroa-Espinoza and Fabre (2011) at different values of surface tension. They have shown that asymmetry means increased bubble velocity and decreased curvature radius in stagnation point at the bubble nose. The same authors (Fabre and Figueroa-Espinoza, 2014) have performed experimental study of symmetry breakup and have shown that asymmetry is rather independent of turbulent or laminar regime. They have found vorticity-to-radius ratio at stagnation point as a crucial parameter for symmetry breakup. Counter-current slug flow was studied also by Fershtman et al. (2017), who have measured liquid velocity that exactly balances the buoyancy $U_L = 0.35\sqrt{gD} = 0.178$ m/s. This velocity is observed also in our experiments. The latest study of the Taylor bubble in a downward liquid flow is by Abubakar and Matar (2022). They have performed detailed numerical analysis and parametric analysis of downward liquid velocity, viscosity and surface tension effects on the shape and bubble motion. A linear stability analysis identified regions of dimensionless parameters within which the bubble is unstable and assumes an asymmetric shape. They have also provided the mechanisms responsible for symmetry breakup. Our experiments are performed in the unstable region with asymmetric bubble shapes, where unstable behavior of the bubble required dynamic flow rate control, which is described in the following section.

Interactions of Taylor bubbles with turbulent liquid flow were topics of various studies. Unlike the laminar liquid flow (Benattalah et al. 2011), in the turbulent background flow the bubble skirt starts to break up and this process and the process of re-coalescence in the bubble wake region can be observed. First such studies were performed by Delfos

et al. (2001a, 2001b) in a pipe with a diameter of 10 cm and later by Kockx et al. (2005). They were measuring gas loss from a Taylor bubble that was held stationary in a counter-current liquid flow. This was achieved with a special spherical Teflon cap, which held the bubble at the fixed position. This was possible as the point of interest in this study was the bubble wake region that is not affected by the placement of the spherical cap. Even in such configuration the bubble's interface in turbulent flow exhibits unstable and chaotic flapping of the bubble tail, which requires long time periods for sufficient statistics accumulation. More recent experiments with the Taylor bubble in the turbulent counter-current regime were performed with high-speed camera in visible light and a disintegration rate of the bubble has been measured (Mikuš et al., 2019). With dynamical liquid mass flow rate control the Taylor bubble stays trapped in the equilibrium position for hours and can be used for studies over time intervals of several minutes. The observed flow conditions are therefore suitable for studying various phenomena, e.g. coalescence and break-up of gas bubbles.

Detailed measurements of the velocity field in turbulent flow around Taylor bubbles is mostly focused on co-current configurations. Pinto et al. (2005) used Particle Image Velocimetry (PIV) technique to precisely measure velocity profiles around the Taylor bubble. They found out that the transition of bubble velocity depends on the Reynolds number of the background liquid flow and proposed replacement of the constant C in Eq. (2) with a function $C = C(\text{Re})$. Shemer et al. (2005, 2007) also performed PIV measurements around the Taylor bubble in a co-current laminar and turbulent flow for different pipe diameters. The study has focused on the impact of the Taylor bubble on the liquid background flow and on the transition between different basic patterns, starting from a complicated version of a circumferential wall jet right behind the bubble to gradually approaching a developed pipe flow, either laminar or turbulent, far away from the bubble. In one of the most recent studies, Cerqueira and Paladino (2020) focused on the interaction between the small dispersed bubbles and the Taylor bubble in a co-current turbulent flow. The flow was analyzed with PIV techniques, high-speed camera imaging and laser diode photocell. The results show that the gas volume fraction of the bubbly background flow affects the terminal Taylor bubble velocity.

Some other experimental techniques are relevant for Taylor bubble studies: an experimental method in development is Electrical Impedance Tomography (De Moura et al. 2021), which represents an invasive technique. This method is able to provide three-dimensional, time dependent shapes of the Taylor bubble in a similar way as wire-mesh sensor techniques (Yoshida et al., 2022). Another experimental technique, which was applied in laminar counter-current flow with stagnant and stable Taylor bubble, was the magnetic resonance imaging by Kemper et al. (2021). The non-invasive method successfully provided three-dimensional fields of the steady state flow near the smooth Taylor bubble tail and has shown reasonable agreement with the two-dimensional PIV measurements. Another three-dimensional method relevant for various two-phase flow, is based on X-ray tomography, which was applied for measurements of horizontal annular flows by Porombka et al. (2021).

Before we move to the main part of this paper, we give a brief overview of another topic of two-phase flow research, which is not directly connected with the previous studies of the Taylor bubble dynamics, but is relevant for our current work. The key novelty of our paper is tracking of the disturbance waves traveling over the interface of the Taylor bubble. Previous studies of disturbance waves on the interfaces were focused on film flow studies and on annular two-phase flow research. Schubring et al. (2010) performed high-speed video camera measurements of individual disturbance wave velocities, lengths and temporal spacing, as well as, average properties, such as frequencies and intermittency (besides average velocity and length). In their work, measured video frames were analyzed with the use of normalized pixel brightness signals obtained from several so-called "virtual detectors" that sampled pixels at different locations. To improve detection for

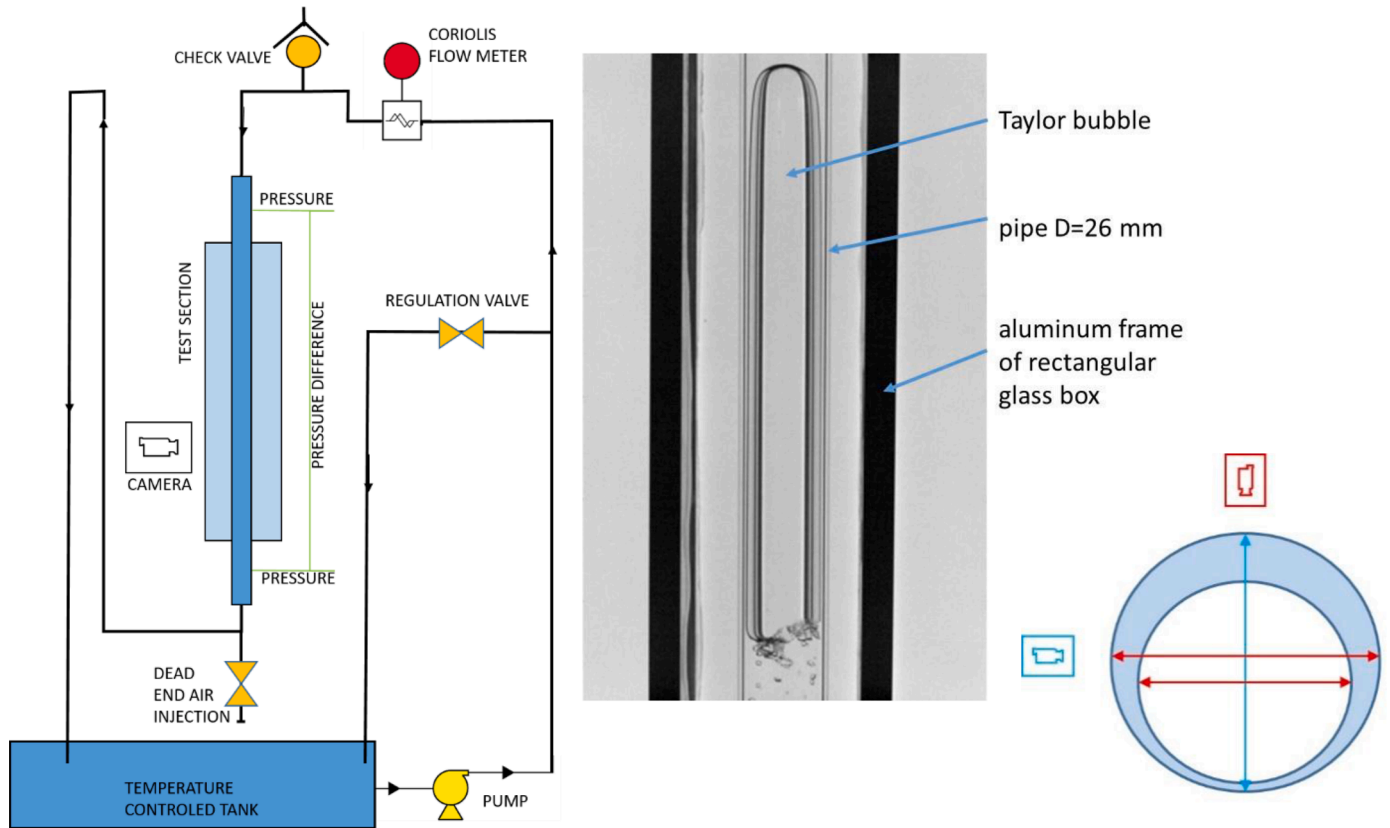


Fig. 1. Schematics of the test loop (left), photograph of the test section during operation (center), and two of the possible bubble positions and dimensions seen on the photographs (right).

waves of smaller peaks, a “wave score” metric was introduced, which adds information on pixel darkness from the preceding and next video frames to the current one. Their measurements were performed in a range of gas velocities between 30 and 80 m/s and liquid velocities up to 50 cm/s, giving wave velocities between 2 and 8 m/s. These values are much larger than the characteristic velocities between 0.1 and 1 m/s in our experiments.

For liquid film waves in co-current horizontal annular flow, Pearce (1979) provided an empirical model for wave velocity that is determined from the liquid surface velocity, gas velocity and gas-liquid density ratio as

$$U_{\text{wave}} = \frac{U_{L,i} + U_G \sqrt{\rho_G / \rho_L}}{1 + \sqrt{\rho_G / \rho_L}}$$

It is probably not adequate to assume the validity of this annular flow correlation for the waves on the Taylor bubble surface, however for the very small density ratio in our air-water two-phase system ($\sqrt{\rho_G / \rho_L} \approx 0.03$), Pearce correlation predicts the wave velocity approximately equal to the velocity measured at the liquid surface, i.e. $U_{\text{wave}} \approx U_{L,i}$. This prediction is in agreement with our results in Section 4.

The film thickness measurements and interface wave analyses in annular flow based on optical techniques were performed also by Pan et al. (2015) in air-water annular flow on a very small scale (70 pixels per mm), and recently by Moreira et al. (2020) in saturated flow of R245fa refrigerant. Similar approach has been taken by Lin et al. (2020), who has also addressed the refraction uncertainty in annular flow, which is relevant also for our Taylor bubble analyses. Ayati et al. (2017) studied forced interfacial waves in stratified turbulent gas and liquid flow in horizontal pipe and reconstructed instantaneous interface positions from the experiment with digital image processing. Obtained surface fluctuations superimposed on the mean liquid height measurement were combined with parallel PIV measurements in liquid phase.

Waves were captured and reproduced well by their technique.

Some other techniques like laser-induced fluorescence (Alekseenko et al. 2014) and Near-Infrared technique (Wang et al. 2018) were also used for studies of interfacial waves in annular flow. Rivera et al. (2022) used point conductance probes to perform dynamic liquid film thickness measurements. Another technique, which provides three-dimensional image of interfacial waves in annular flow is to be mentioned: Fershtman et al. (2020) used a multilayer conductance sensor to obtain three-dimensional spatial and temporal information on interfacial wave structures in upward annular flow in vertical and inclined pipes. They have observed three types of interfacial structures: ripples, disturbance and rogue waves, where the amplitude of the waves was the main property used to differ between the waves. The methodology has been further refined by Fershtman et al. (2021). They have observed experimentally the interfacial ripples and disturbance waves in annular flow in upward inclined pipes. Non-intrusive liquid film sensor measurements were used together with methods for identification of individual waves and differentiation between ripples and larger waves. They observed a bi-modal distribution of wave heights, where first mode corresponds to ripples and the second to disturbance waves, which enabled a clear differentiation between the two types.

Numerical simulations of the Taylor bubble are not directly relevant for the present work, however we have performed our experiments with a view on the high-resolution numerical simulations with explicit interface tracking that will be able to reproduce our measurements. Most of the numerical studies were performed in a stagnant or co-current background liquid flow in a variety of settings, from simple two-dimensional and Euler-Euler simulations to the fully three-dimensional simulations with interface tracking. Mao and Dukler (1991) performed one of the first simulations of the Taylor bubble. They have also performed experiments in the co-current regime and stagnant liquid. These experimental data were then compared with two-dimensional

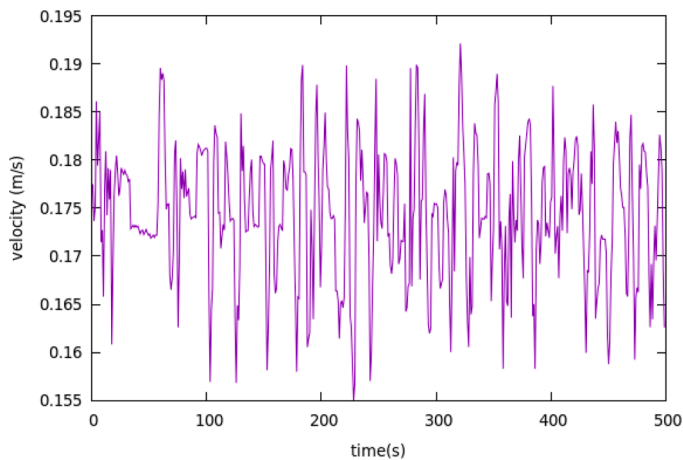


Fig. 2. Mean liquid velocity in the test section upstream of the Taylor bubble computed from the measured mass flow rate, case 2D-10(1) in Table 1. Time averaged value: 0.175 m/s.

simulations, where the main focus was placed on the correct prediction of the bubble shape and rise velocity. Araujo et al. (2012) performed two-dimensional numerical simulations of individual Taylor bubbles rising through vertical columns of stagnant Newtonian liquid in laminar flow regime. They have used Ansys FLUENT computer code with Volume-of-Fluid (VOF) method. The simulations covered wide ranges of Morton and Eotvos numbers and classified the hydrodynamic properties of the bubble wake, liquid film and nose region as functions of surface tension, Froude and Morton numbers. In recent years, there was a rise of three-dimensional simulations of the Taylor bubble. Gutiérrez et al. (2017) simulated the rise of Taylor bubble in a stagnant liquid using level-set/moving mesh method. Frederix et al. (2020) and Mikuž et al. (2020) performed large eddy simulations alongside the VOF interface tracking solver of the Taylor bubble in co-current turbulent flow. They have used Runge-Kutta time integration, moving frame of reference which followed the Taylor bubble motion, and mapping of the inlet velocity boundary to ensure the fully developed turbulent flow. As the bubble undergoes shedding, additional models for coalescence and break-up should be incorporated into the simulations. In another study Cerqueira et al. (2021) also performed CFD simulations of the problem, where they used coupling of the VOF method for the modelling of large-scale interface dynamics and the Discrete Bubble Model (DBM) for modelling the small-scale bubbles. The results were compared with experimental results. CFD results confirmed that the presence of small dispersed bubbles increases the terminal velocity of the Taylor bubble. Rohilla and Das (2020) have performed experimental and numerical study of an impact of a Taylor bubble on a single smaller bubble in a rectangular column. They have studied also the influence of Morton number on the behavior of a single bubble and differentiated it into sprint-away regime and bubble slip regime. Number of studies were done also in annular geometry, which is relevant in petrochemical industry. In two recent studies Liu et al. (2023) and Lou et al. (2022) have performed experimental and numerical studies of Taylor bubble in a pipe of annular cross-section. Wide range of dimensionless numbers of Taylor bubble in upward and downward flows was investigated by Lizarraga-Garcia et al. (2021) with level set method implemented in a commercial code. One of the most recent studies was performed by Wang et al. (2023), who have studied accelerated Taylor bubbles with a combination of Level-Set and VOF methods. Similar problem was successfully approached with lattice Boltzmann method by Mitchell and Leonardi (2020).

The structure of this paper, which is focused on the Taylor bubble shape and disturbance waves traveling over its body in a counter-current turbulent flow, starts with Section 2. dedicated to the description of the experimental loop and instrumentation. The most general results on the

Taylor bubble shape and typical timescales of bubble instability are provided in Section 3. The main contribution of the paper in Section 4 is focused on the measurements of propagation velocities of the interface waves, possibilities and limitations of our velocity measurement technique, which are further discussed in the concluding Section 5. In Appendix A, a brief overview of the algorithms used in the image analysis is given and in Appendix B further analysis of bubble instability is given.

2. Experimental device and instrumentation

The experiments were performed in a loop shown in Fig. 1. The key part of the loop is a test section of 1.5 m long glass pipe with internal diameter $D = 26$ mm. Water temperature was maintained constant at temperatures between 20 and 30 °C with a heat exchanger in the tank and the mass flow rate was measured with a frequency of 1 Hz with Coriolis flow meter. All experiments were performed in turbulent flow regime of the liquid above the bubble with Reynolds number around 6000 based on superficial liquid velocity. The straight section of the pipe above the bubble was around 40 diameters long, and was found to be sufficiently long to obtain statistically uniform turbulence above the nose of the bubble. Taylor bubble was introduced into the test section from the dead end pipe installed under the test section. Flow through the test section was manually regulated with a control valve that was adjusting the distribution of the flow between the main loop and a bypass loop. To keep the bubble within a camera field of view, manual adjustments of the flow rate were typically made every couple of seconds.

Taylor bubble was observed with a high-speed camera with a field of view that captured 20 cm (~ 8 diameters = $8D$) long section of the pipe in the first measurements and was later reduced to 14 cm ($\sim 5D$) section for the main measurements in the present paper. The pipe was surrounded with a rectangular glass section filled with water, which has minimized the optical distortion. Useful resolution of the camera in the main measurements was around 1280×240 pixels or approximately 9 pixels/mm. The lengths of the observed Taylor bubbles were typically between 1.5D and 5D, although we had problems to retain the bubbles above 4D lengths within the camera field of view over several minutes of recording. Measurements in this work were performed over 8, 4, 2, and 1 min time intervals at camera frequencies 100, 200, 400 and 800 Hz, respectively.

Taylor bubble photograph seen in Fig. 1 (center) provides information about the inner diameter of the glass pipe and the outer diameter of the air bubble. As seen in the right image of Fig. 1, this information does not depend on the eccentric position of the bubble in the pipe. Thus, as long as the bubble cross-section is of circular shape, we measure its diameter from an arbitrary direction; in other words, blue and red cameras in the right image of Fig. 1 provide the same information. The same image also clarifies our "definition" of the liquid film thickness seen from different directions; the liquid film thickness obtained from two-dimensional photographs, is a difference between the pipe wall and the outer-most points on the bubble perimeter. As will be discussed in Appendix B, the cross-sections of the bubbles are indeed very close to the ideal circular shape at distances of at least 1 pipe diameter downstream the bubble nose.

Optical distortion of the liquid film thickness measurement is estimated to be low (Pan et al., 2015 and Lin et al., 2020). Absolute film thickness is measured with a precision between 0.5 and 1 pixel, which means relative errors more than 40% for the very thin films below 3 pixels thickness. Optical distortion is estimated with the geometrical optics and enlarges the liquid film thickness for up to 2%, which is significantly less than uncertainty of the interface reconstruction.

The instability of the Taylor bubble in the counter-current flow configuration requires dynamic changes of the mass flow rates in the experiment to keep the bubble within the camera field of view. Minor manual corrections of the valve positions are required every few seconds

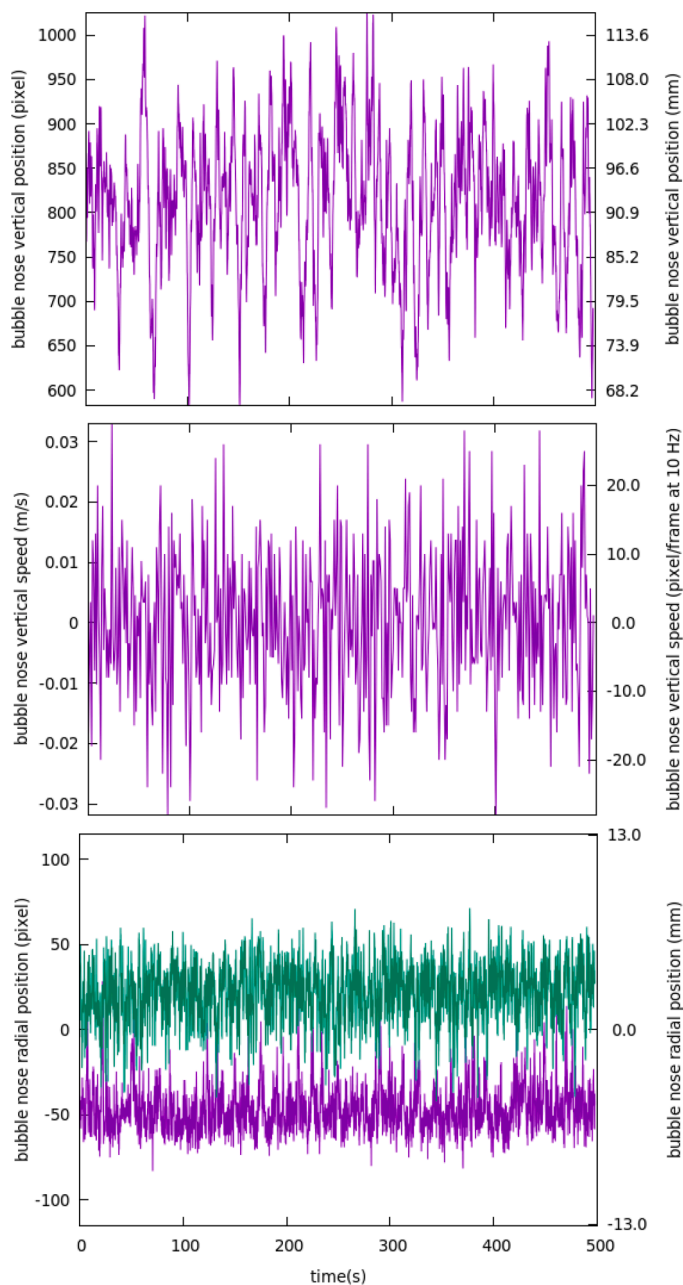


Fig. 3. Top: typical bubble nose vertical position measured from the bottom line of the camera field of view. Middle: bubble nose vertical velocity. Bottom: distance of the bubble nose from the pipe axis for two typical measurements (2D-10(1) and 2D-10(2) in Table 1).

and the resulting bulk liquid velocity in the test section obtained from Coriolis flow meter readings, during 8 min interval of typical experiment is shown in Fig. 2. Statistical dispersion (Root-Mean-Square) of the velocity signal shown in Fig. 2 is 4% of the bulk velocity. The range of statistical dispersions in other experimental cases is between 3% and 10% of the bulk velocity. These fluctuations are roughly one order of magnitude larger than the flow rate fluctuations due to the turbulent nature of the single phase channel flow obtained in our Direct Numerical Simulation (DNS) studies at constant pressure gradient boundary conditions performed in computational domains that were around 5 hydraulic diameters long (Bergant and Tiselj, 2007).

The manual flow rate adjustment technique for the bubble position control might seem to be problematic for comparison with similar experiments or numerical simulations. However, it is actually similar to

the numerical technique used in high-fidelity numerical simulation of co-current Taylor bubble flow of Frederix et al. (2020). They modelled the Taylor bubble in a moving frame of reference, like Taha and Cui (2006), but they have also included minor changes in the inlet velocity at each time step. These slow changes of bulk liquid velocity were needed to keep the bubble inside their computational domain.

2.1. Image processing

The main data analyses in our experiments are based on processing of roughly 50,000 photographs taken in each experimental case. The image processing provided shapes of the Taylor bubble interface on each instantaneous photograph. We have performed this task with a newly developed in-house software that relies on widely used libraries available in the open domain. An overview of the algorithms used to extract the Taylor bubble's interface from the photographs is given in the Appendix A. At this point it is sufficient to write that the interface reconstruction was performed in two steps:

- 1) A rough reconstruction of the Taylor bubble interface was first performed on the pixel level.
- 2) A local information around each pixel identified in the first step is used to refine the position of the interface in the second step to a sub-pixel level.

For the further discussion it is important to make a distinction between the absolute and relative accuracy of the interface recognition that was achieved in our image processing. Absolute uncertainty of the interface position in a single point on a single photograph is between half a pixel and one pixel. However, when time series or spatial profiles of the interface are recognized, the relative uncertainty of the interface motions between the pixels that are neighbors in space or time is reduced for a factor of around 5 to approximately ± 0.1 pixel. The absolute uncertainty is relevant for the analyses of the bubble shape and for measurements of the liquid film thickness at the boundary of the Taylor bubble. The relative uncertainty is relevant in analyses of the waves traveling over the surface of the Taylor bubble.

3. Results - analyses of time averaged Taylor bubble shape

3.1. Vertical and horizontal movements of the Taylor bubble

While we claim that our bubble is at fixed vertical position, this is not entirely true due to the unstable nature of the Taylor bubble in the counter-current flow, the chaotic nature of the turbulent flow and consequently minor unsteadiness of the flow rates in our loop. During the measurements we kept the bubble in the observation region with manual adjustments of the mass flow rate. The vertical movements of the typical Taylor bubble in our experiments are shown in top two graphs of Fig. 3. Detailed comparison of the bubble vertical position in the top image of Fig. 3 shows that the position is correlated with the mass flow rate time history shown in Fig. 2. This is of course a natural consequence of the manual flow rate adjustments needed to keep the bubble inside the camera field of view, where valve operator followed the vertical position of the bubble. Vertical velocity of the bubble computed from the positions measured at 10 Hz effective frequency (basic recording frequency was 100 Hz with 1 out of 10 images stored), is shown in the middle image of Fig. 3. Typical vertical velocity of the bubble is around 0.01 m/s, which is low comparing to the 0.18 m/s mean liquid velocity upstream of the bubble and around 1 m/s velocities on the liquid-air interface of the Taylor bubble.

The bottom image of Fig. 3 shows radial position of the bubble nose during two 8 min measurements. Axisymmetric bubble nose would be fixed at the axis at $r = 0$, however, what one can see in this image is quasi-stable asymmetric position of both bubbles. In the particular case of the two bubbles shown in the Fig. 3 bottom, one of the bubbles is

Table 1
Experimental cases by names, camera frequency and bubble length.

Measurement case	Camera frequency (Hz)	Bubble length (D pipe diameter)
8*2D-10 (8 separate cases)	100 (effective 10)	2D
2D-200	200	2D
2D-400	200	2D
4D-200	400	4D
4D-400	400	4D
4D-800	800	4D

inclined to one side of the two-dimensional projection and the other one to the other side. The noses of both bubbles cross the axis from time to time, however in the average, they remain attached to one side of the pipe during the 8 min time interval. Under the conditions of our experiments, this asymmetry is very persistent and our empirical observations show that once the bubble has "chosen" the particular side of the pipe, it typically remains there for a very long time, despite occasional movements in radial direction. The same behavior was observed for all other bubbles considered in the present study and in some other cases that were not included in this paper: asymmetric position and azimuthal orientation of the bubble, which was attained at the beginning of the experiment when the bubble was injected into the pipe, remained unchanged during the measurement. Consequently, our two-dimensional photographs were affected by the azimuthal position of the bubble with respect to the direction of the camera. We have checked possible asymmetries of our experimental device to find a possible preferential position of the Taylor bubble, however, we did not identify such asymmetries and the bubble positions in various experiments were actually observed at all azimuthal angles of the pipe. The issue of asymmetry is further studied in the next Section 3.2.

3.2. Time averaged bubble shape

The initial goal of our research was to predict time averaged Taylor bubble shape in the counter-current turbulent flow, which could be useful for validation of CFD models that are being developed to study the same phenomena (Coste, 2013). However, as already shown in the bottom image of Fig. 3 and discussed in the Section 3.1, we cannot obtain axisymmetric time averaged images of the Taylor bubble. We cannot entirely exclude the possibility that a particular bubble will significantly change its azimuthal orientation in the pipe, however, we did not observe this phenomenon in around 20 analyzed Taylor bubbles.

We have restricted our measurements to time intervals of up to 8 min due to the decay of the Taylor bubble. Mikuz et al. (2019) have shown that small bubbles, which break-up from the tail of the Taylor bubble, set the lifetime of the Taylor bubbles of the 4D length to around one hour. Thus, we have combined time averaging and ensemble averaging to obtain a less skewed shape of the time averaged bubble. For ensemble averaging we have performed a series of eight measurements, denoted as 2D-10 cases in Table 1, at effective 10 Hz camera frequency (100 Hz measurements with 1 out of 10 images stored) and 8 min time intervals. All eight measurements were performed at similar conditions with the length of observed Taylor bubbles around 2D. Time averaging was performed for each case and the cases were later merged with ensemble averaging into a single set of data shown in Fig. 4. These cases are denoted as a single case "8*2D-10" in Table 1. Four different bubbles were studied in these eight measurements. Most of the small images in Fig. 4 show asymmetric time averaged bubble interface, and even the bottom-left pair of small images, which shows symmetric time averaged silhouettes, was not symmetric but tilted towards or away from the camera plane of view. Ensemble averaged bubble shape shown in large image of Fig. 4 exhibits better axial symmetry than most of the particular

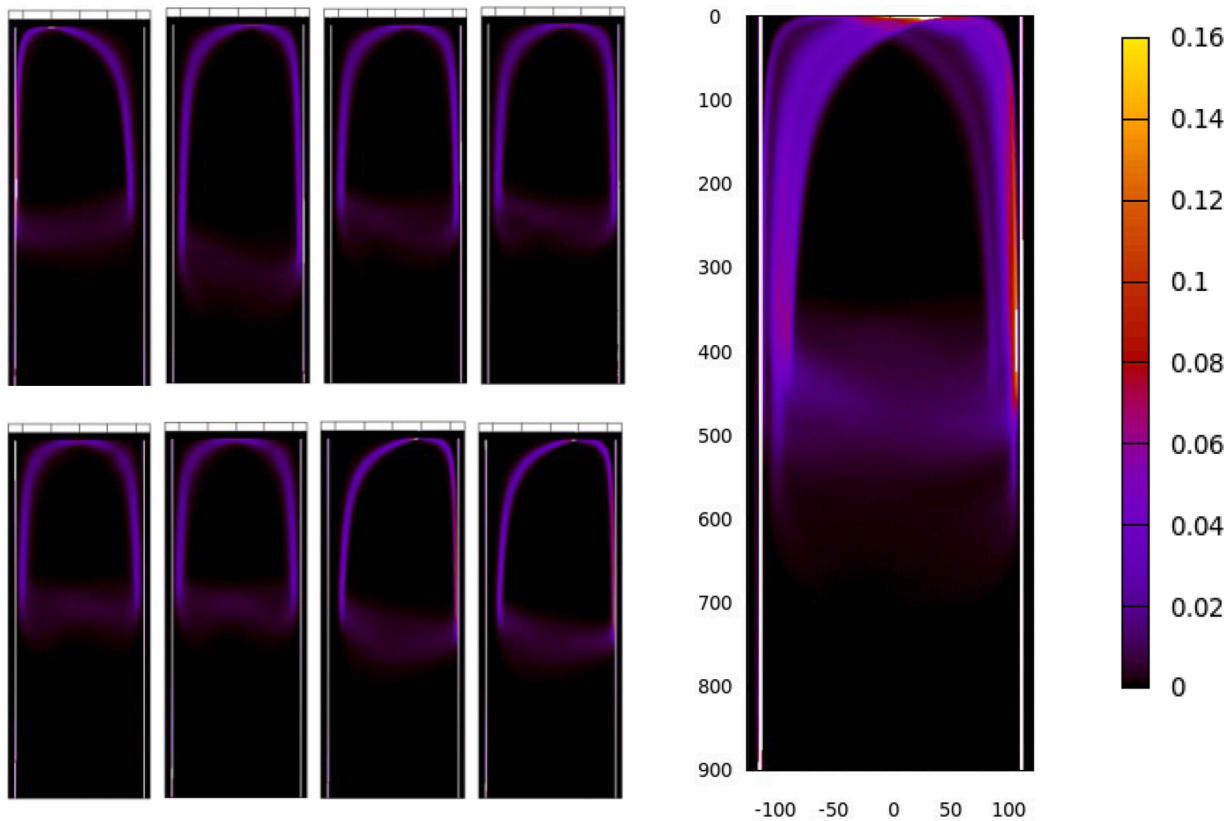


Fig. 4. Eight small images: time averaged Taylor bubble interface position from eight measurements (8 min, 5000 photographs each). Large image, 8*2D-10 case: Taylor bubble interface position obtained with ensemble average of eight time averaged fields. Color scale: share of photographs with interface location at the given pixel position (maximum = 1). All units on horizontal (r) and vertical (z) axes are given in pixels.

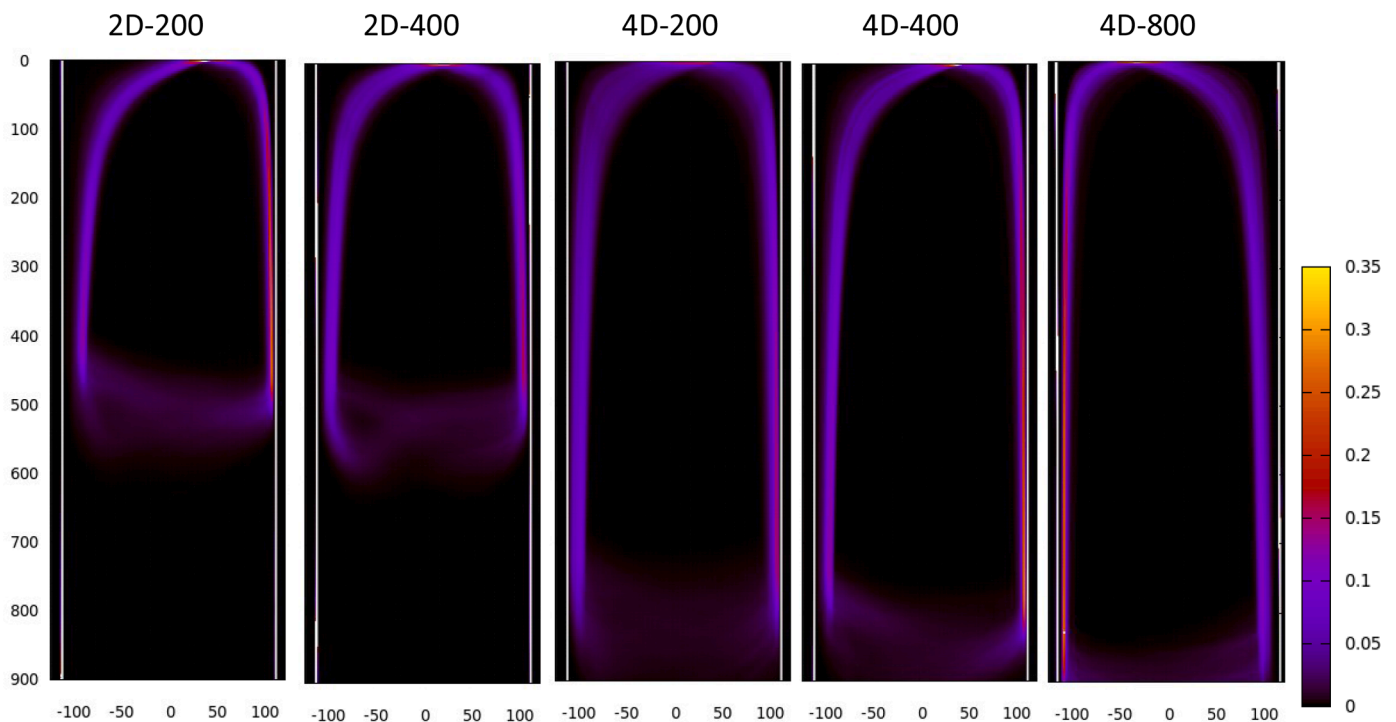


Fig. 5. Time averaged (4, 2, or 1 min, 50,000 photographs) Taylor bubble interface position for 2D and 4D bubbles. Color scale: share of photographs with interface location at the given pixel position. Units on horizontal (r) and vertical (z) axes are given in pixels.

bubbles shown in small images of Fig. 4, however, even this time plus ensemble average is tilted towards the right wall. Consequently, the axisymmetric time-averaged Taylor bubble shape is not a viable scenario under conditions of our experiment. Additional ensemble averaging can possibly result in improved axial symmetry, however, such approach is questionable, since any numerical simulation or similar experiment should eventually produce asymmetric time averaged results, if time averaging is used without ensemble averaging. As our measurements show, the ideal visual observation should be based on three-dimensional images of the Taylor bubble taken from different angles, where the azimuthal orientation of the eccentric bubble (shown in right drawing of Fig. 1) would be identified before further data processing.

During the averaging shown in Fig. 4, the axial (z) positions of the bubble on each photograph were shifted for an appropriate distance that moved the bubble nose into the same axial point at position 0 pixels and the axial distance is measured downward from the bubble nose. This procedure gives a special meaning to the bubble nose point, which is not entirely deserved: more appropriate time averaging would be obtained with axial shifting of the bubble position with respect to the center of mass of the observed bubble. However, to obtain the center of mass for three-dimensional bubble or for its two-dimensional silhouette, the complete bubble interface must be reconstructed. Due to the flapping and highly asymmetric shape of the bubble tail, where the bubble is slowly losing its mass through decay with the detachment of small bubbles, we have abandoned this approach. Even if we were able to do it, the center of mass of two-dimensional silhouette is not the same as the physical center of mass of the bubble. Consequently, since the center of mass cannot be computed from the silhouette photographs with high accuracy, and the wobbling of the bubble nose in axial direction is rather mild, we have kept the nose point as a reference point for the purpose of the present study. Fig. 5 shows other five test cases analyzed for the present paper. Five different Taylor bubbles of 2D and 4D length were time averaged over 1, 2 or 4 min time interval with frequencies 800, 400 and 200 Hz, respectively. Color intensity in particular pixel in the r - z plane corresponds to the number of photographs where the interface was located in the particular pixel of the plane. Like in the Fig. 4, time

averaged shapes of these bubbles do not exhibit axial symmetry.

Detailed insight into the images of Figs. 4 and 5 shows also the position of the bubble's tail. Nevertheless, this information is irrelevant and is merely an artefact of our bubble interface reconstruction algorithm, which recognized the bubble's tail on some of the photographs. However, the quality of the tail reconstruction was not verified or tested and should not be considered as a relevant result of the present study.

Time averaged bubble shapes presented in this Section were against our initial expectations that asymmetry will disappear after sufficiently long time averaging. The reason was not in experimental uncertainties, but in the physics of the Taylor bubble in the counter-current turbulent flow. Quasi-stable asymmetries of the bubble positions, which are typically observed over several minute time intervals, result in asymmetric time averaged bubble shapes. Since the azimuthal position of the asymmetric bubble seems to be determined during the injection of the bubble into the test section, one would need three-dimensional information for comparison of different bubbles from different measurements. Consequently, our attempt to produce axisymmetric time averaged plus ensemble averaged bubble shapes results in a loss of information in azimuthal direction and thus contains significant statistical uncertainties, which might be too large for detailed comparisons with similar experiments or with high fidelity simulations. Nevertheless, useful results are obtained with averaging of the bubble shape and corresponding liquid film thickness over both sides of the photographs. This approach results in relatively accurate liquid film thickness, which is showing reasonably small statistical dispersion among various Taylor bubbles and is discussed in Appendix B.

The problem of ensemble averaging is in the fact that it enforces axial symmetry, which does not exist in our flow conditions. Ideal averaging of the three-dimensional bubble shape would require stereoscopic measurements and recognition of the three-dimensional bubble shape. Such approach would eventually result in an asymmetric bubble shape that would be directly comparable to possible future measurements or three-dimensional simulations.

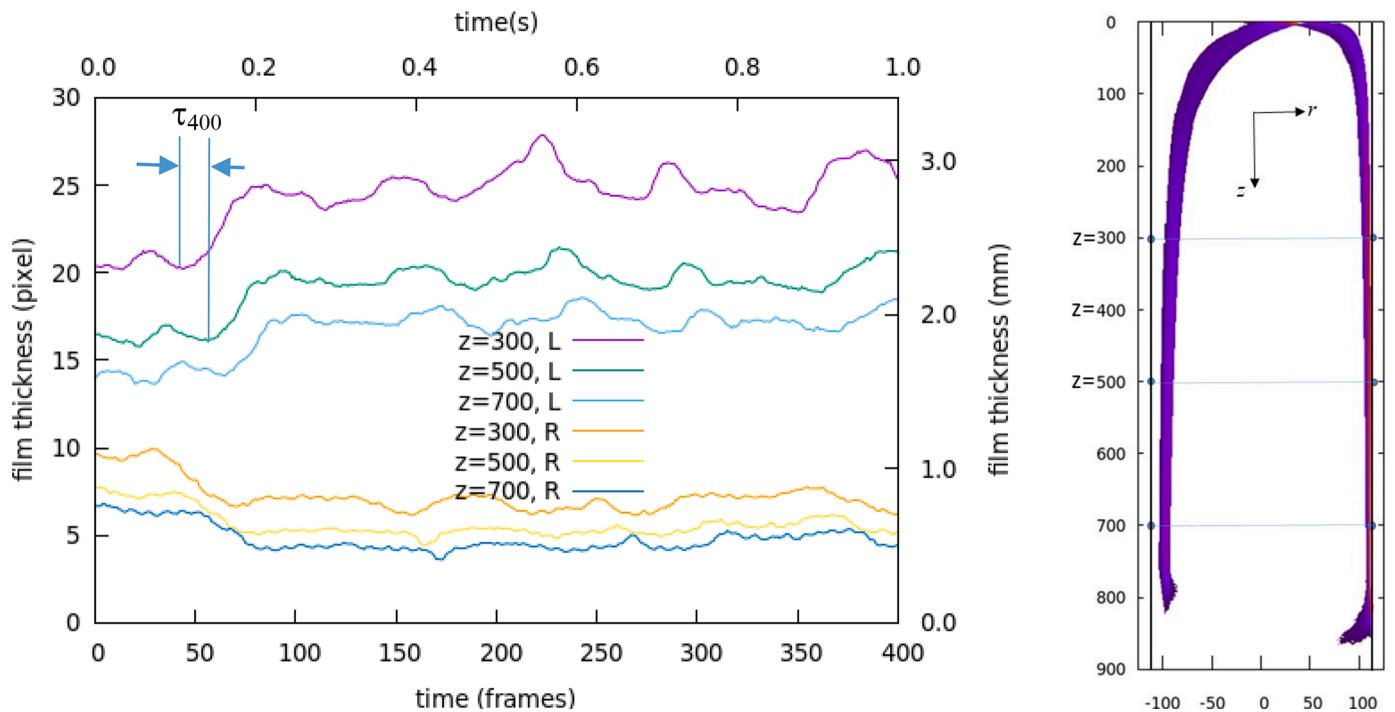


Fig. 6. Liquid film thickness time history at 6 points along both sides of the 4D-400 bubble. Legend: z coordinate of the measuring point in pixels, L - left side film, R - right side film.

Table 2
Characteristic wavelengths λ , frequencies ν and phase velocities c of relevant capillary waves.

film thickness d (mm)	λ (mm)	ν (Hz)	c (m/s)
very thin 0.1	2	100	0.2
very thin 0.1	100	0.05	0.005
average thin film 0.5	5	40	0.2
average thick film 2	50	1	0.05
very thick 10	2	200	0.5
very thick 10	100	0.5	0.05

4. Results - propagation of disturbance waves on Taylor bubble surface

The main contribution of our research is presented in this Section. It is based on the ability of our measurement techniques and image processing algorithms to track small disturbance waves traveling along the Taylor bubble interface. An example of such waves is shown in Fig. 6. The mechanisms, which generate the interface waves recognized in our experiment are mainly attributed to the turbulence in the incoming liquid flow, flow rate fluctuations, or instability of the Taylor bubble in the counter-current flow. Some of them might be induced by the vibrations of the test section structure, air moving inside the bubble, and some of them, which would be expected to travel upward, might be produced by the flapping tail of the bubble. The later waves were studied by Liberzon et al. (2006) for shorter bubbles. Most of the waves produced by the random disturbances are expected to travel in all directions parallel to the air-water interface with velocities that are governed by the capillary wave equations written for the moving pair of liquids. We cannot totally exclude mechanisms, which might generate non-isotropic waves, however, we assume that they are not relevant. According to Liberzon et al. (2006) the dispersion relation of capillary waves is

$$\omega^2 = \frac{\sigma}{\rho} k^3 \tanh(k d),$$

with wave number $k = 2\pi/\lambda$, angular frequency $\omega = 2\pi\nu$, and phase velocity $c = \lambda\nu$. If we assume that it is approximately valid for the liquid film of thickness d near the Taylor bubble, we can estimate the characteristic values of the disturbance waves in our system (Table 2).

Characteristic wavelengths in our experiment can range from roughly $\lambda = 2$ mm, imposed by the resolution of our photographs, to around 10 cm, which is the length of our 4D bubbles. The liquid film thickness d spans from around 0.1 mm (~ 1 pixel) to 1 cm. For liquid density $\rho = 1000$ kg/m³ and surface tension $\sigma = 0.07$ N/m the relevant frequencies and phase velocities of the capillary waves are collected in Table 2 (rounded to a single digit). Extreme values of parameters are estimated for the very thin and very thick films, while the values in bold are given for films that were most frequently observed in the measurements. Further analyses of measurements performed at camera frequencies of up to 1600 Hz have shown that all relevant phenomena captured in the system appear at frequencies below ~ 100 Hz. It is important to emphasize that the estimated phase (and group) velocities of the resolved waves are lower or equal to the mean film velocity estimated to be between 0.5 and 1 m/s. That estimate means practically all waves on the interface travel downward. The only measurable exceptions were short wavelength and high frequency disturbance waves generated at the tail of the short bubbles of length $2D$, which traveled a few mm upstream. These waves were invisible in longer bubbles of $4D$ length.

4.1. Disturbance waves velocity - measurement technique

Fig. 6 shows a short time interval with time development of liquid film thickness in two triplets of points along the z axis of the 4D-400 bubble. Positions of these points are shown in auxiliary drawing in Fig. 6. Similarity of the profiles on the same side of Fig. 6 is rather obvious and one can also see a time lag between the signals measured in the points 300 pixels downstream the bubble nose, and lower points at 500 and 700 pixels downstream. Especially the oscillations at the left side of the Taylor bubble where the film is thicker, show very clear trend of film thinning and travelling of the liquid-air interface disturbance waves in the downstream direction. The same trend, just slightly less

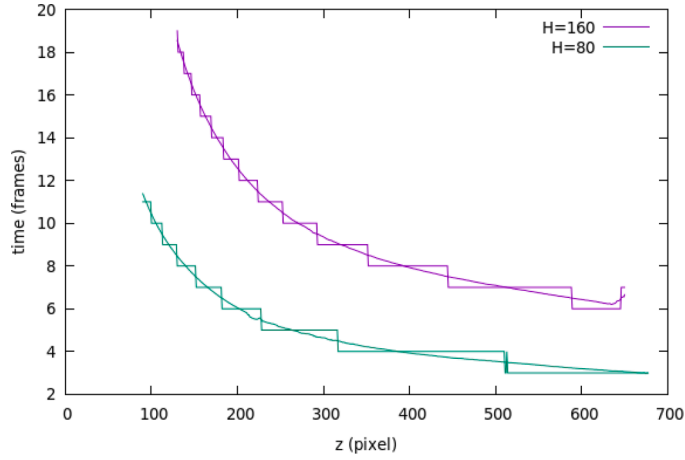


Fig. 7. Time lag of interface disturbance waves measured in frames for $H = 80$ and $H = 160$ pixels for left side liquid film of the 4D-400 case. Step curves: maximum cross-correlation time lag τ , continuous curves: time lag τ refined with parabolic interpolation. 8.8 pixels = 1 mm, 400 frames = 1 s.

pronounced and with more noise from interface reconstruction, is seen also in the points at the right side of the film. The key question that we try to answer below is, what is the observed axial velocity of the disturbance waves travelling over the interface in the downstream direction?

Measurements of the axial disturbance waves velocity w are performed with cross-correlations of the time signals at various axial positions along the pipe. For a chosen distance H between the particular points in space, for example $H = 200$ pixels in Fig. 6, velocity w is obtained from the measured time lag τ of the signals as $w = H/\tau$. For example, the time lag τ_{400} at the point z_{400} (400 pixels downstream the bubble nose) and at distance $H = 200$ pixels, approximately sketched in graph of Fig. 6, is computed from the cross-correlation of time signals at points $z_{400-H/2} = 300$ pixels and $z_{400+H/2} = 500$ pixels. If time development of film thickness at the grid point $z_i = i$ is denoted as $d_i(j)$ and j denotes time and N number of photographs in a given experiment, the cross-correlation coefficient R at that point is obtained as a function of time lag τ as

$$R_i(\tau) = \left(\sum_{j=1}^{N-\tau} d'_{i-H/2}(j) d'_{i+H/2}(j+\tau) \right) / \left(\sum_{j=1}^{N-\tau} d'_{i-H/2}(j)^2 \sum_{j=1+\tau}^N d'_{i+H/2}(j)^2 \right),$$

where $d'_i(j)$ represents the fluctuating part of the film thickness $d_i(j)$ with subtracted time averaged mean value $d'_i(j) = d_i(j) - \bar{d}_i$. The time lag τ_i at position z_i is found as a value of τ with the maximum value of discrete cross-correlation coefficient function $R_i(\tau)$.

Fig. 7 shows two graphs with time lag τ measured in frames at 400 Hz camera frequency on 2 min time interval (125 s = 50,000 frames). Step curves in Fig. 9 show discrete time lags computed at each axial point z_i at distance $H = 80$ pixels (bottom curve) and $H = 160$ pixels (top curve). For example, the time lag of the step curve located in the point $z_i = 140$ pixels and at distance $H = 80$ pixels, is computed from the cross-correlation of time signals in points $z_i = 140-80/2 = 100$ pixels and $z_i = 140+80/2 = 180$ pixels. The next time lag at $z_i = 141$ pixels is obtained from cross-correlation of signals at $z_i = 101$ and $z_i = 181$ pixels, and so on for the points from around $z_i = 100$ and towards the tail of the bubble.

Smooth curves in Fig. 7 represent the time lag τ improved with interpolation among the cross-correlation coefficients of discrete function $R_i(\tau)$: interpolated maximum was determined from a parabola drawn through the time lag τ_{max} with the maximal cross-correlations coefficient and the two cross-correlation coefficients at the two neighboring time lags: $\tau = \tau_{max} \pm 1$ frame. As shown in Fig. 7 and from other

computations, interpolation of the time lag is useful even for very short discrete values of time lag τ , where time lag is down to about one or two frames.

Distance H between the two points, where cross correlation is computed, should not be too short to ensure sufficiently long time lag between the signals in both points at given frequency of the camera. This time lag should be at least a couple of time frames long to achieve a reasonably accurate velocity prediction. Too large distance H is also detrimental, since we can expect dissipation of the disturbance waves that reduces the cross-correlation of the signals over larger distances.

Waves traveling along the nose of the bubble downstream to a distance of about one radius of the pipe from the nose (~ 100 pixels) are propagating along the curved interface. In our analysis, we compute the curved interface length and we use it in evaluation of the velocities, but we take into account only part of the amplitudes that are perpendicular to the pipe axis, which slightly reduces the accuracy of the signals. However, this approximation is rather irrelevant because we focus on the interface waves traveling on a well-defined thin film from the distance of the pipe radius $D/2 \cong 100$ pixels from the bubble nose, downstream to the end of the bubble. This region of the liquid film can be safely considered as a liquid layer with waves traveling in axial (and azimuthal) direction with their amplitudes moving in the radial direction.

4.2. Velocities of disturbance waves - results of measurements

Fig. 8 shows velocity profiles of the disturbance waves along the five Taylor bubbles shown in Fig. 5 obtained from the time lags. Solid lines show velocities on the right side of the bubble and dashed lines show the velocities measured on the left side. The complete time histories (50000 frames) are analyzed in all cases, which means 1, 2 and 4 min for 800, 400, and 200 Hz measurements, respectively. Cross-correlations are compared at different distances from $H = 40$ pixels to $H = 80$ and $H = 160$ pixels.

Thick yellow curves are added in each graph of Fig. 8, which represent time and left-right averaged liquid-air interface velocity. This was approximated from the measured liquid film thickness $h(z)$ and continuity equation as

$$v_i(z) = 1.15 v_0 R^2 / [2Rh(z) - h(z)^2].$$

The approximate relation between the liquid-air interface velocity and the mean liquid film velocity $v_i = 1.15 v_{film-mean}$ follows from our DNS results obtained in infinite turbulent flume flow at similar Reynolds numbers (Bergant and Tiselj, 2007), where the ratio between maximum and average velocity is approximately 1.15. The factor of 1.15 is valid for the free liquid surface near the infinite flat wall and neglects the air shear force. A single uncertainty bar is given for the yellow curve obtained from the continuity equation. This uncertainty is based on absolute uncertainty of the film thickness measurement and interface recognition, which is around 1 pixel and dominates other types of uncertainties.

What we see in Fig. 8 are two types of velocity profiles obtained from the same measurements but with entirely different analysis: yellow curves are obtained directly from the simple measurement of the absolute liquid film thickness combined with continuity equation and the empirical correction coefficient 1.15, while the disturbance wave velocities are obtained from the relative motions of the liquid-air interface. What we can see is remarkable similarity of both types of velocities. Consequently, we claim that the time averaged velocity of the disturbance waves on the water-air interface actually shows the velocity of the interface itself. This observation is considered to be the central result of our present research.

An important question is how to explain equivalence of the time averaged velocities of interface waves with the convective velocity v_i of the interface and apparently absent contribution of the capillary waves

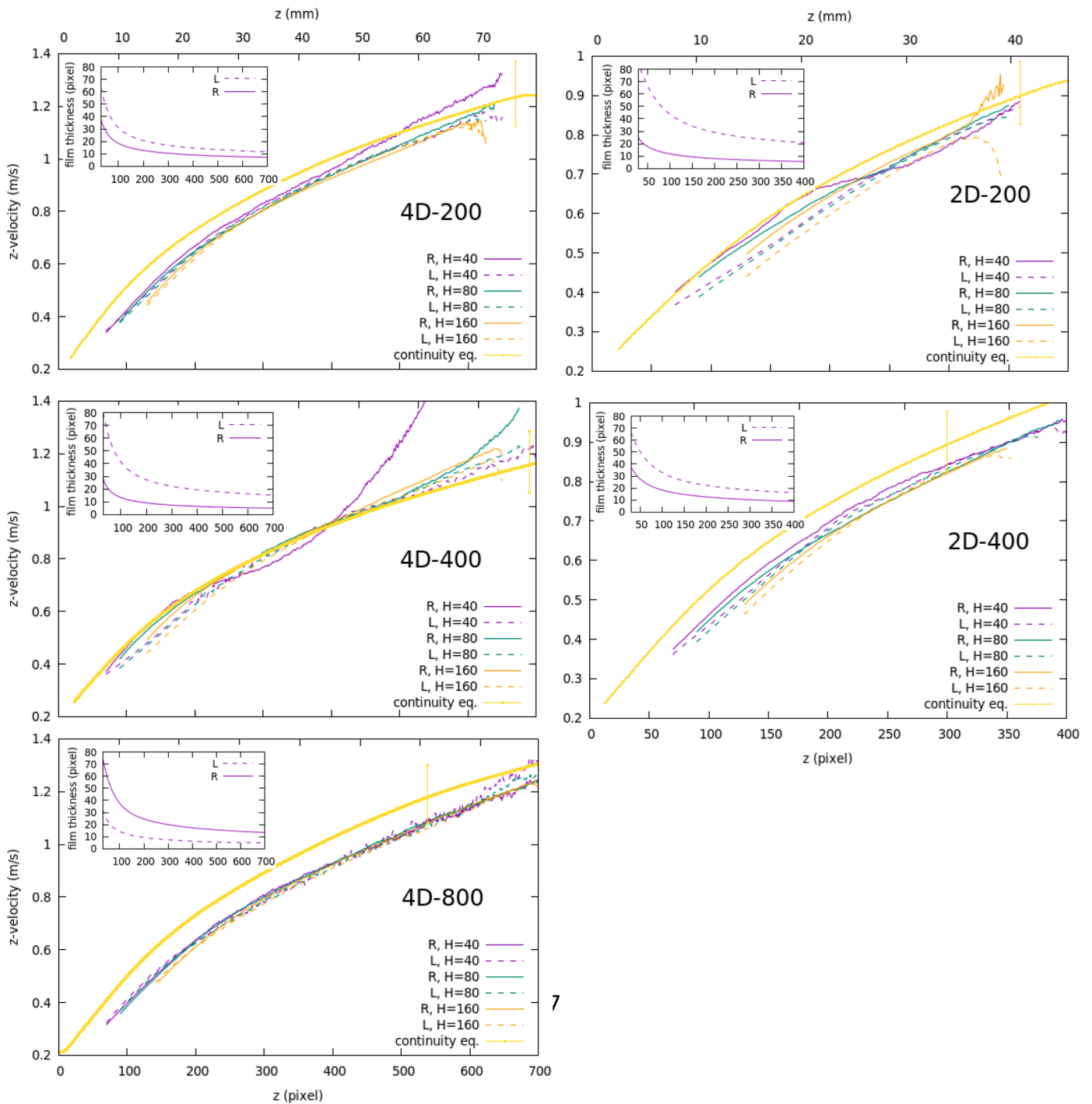


Fig. 8. Velocity of the interface disturbance waves on two sides of the five bubbles (right side film: solid, left side film: dashed). Thick yellow: interface film velocity v_i from measured film thickness and continuity equation. X-axis: distance from the bubble nose. Inset graphs: time averaged left- and right-side film thickness.

that are supposed to travel along the surface in all directions. Sufficiently long time signals contain capillary waves of all frequencies that can propagate in all axial and azimuthal directions. On the videos these waves are allowed to propagate in axial direction with velocities:

$$v_i(z) \pm c_{capillary}(\nu)$$

with interface velocity v_i around ~ 1 m/s in the sufficiently thin region of the liquid film, and $c = c_{capillary}$ as the phase velocity of the capillary surface waves, which is a function of the wave frequency. The equivalence of the time-averaged velocities of interface waves with the interface convective velocity v_i , which is observed in our experiments means

that:

$$\langle v_i(z) \pm c_{capillary}(\nu) \rangle = \langle v_i(z) \rangle,$$

where " $\langle \rangle$ " is used to denote time averaging. We assume two reasons for the equivalence:

- 1) As seen from the values of the characteristic phase velocities $c_{capillary}$ in the Table 2, the velocities of the dominant capillary waves (~ 0.1 m/s) are at least an order of magnitude lower than the interface velocities (except in the nose region of the interface). Consequently, all disturbance waves recognized in the thin region of the film are

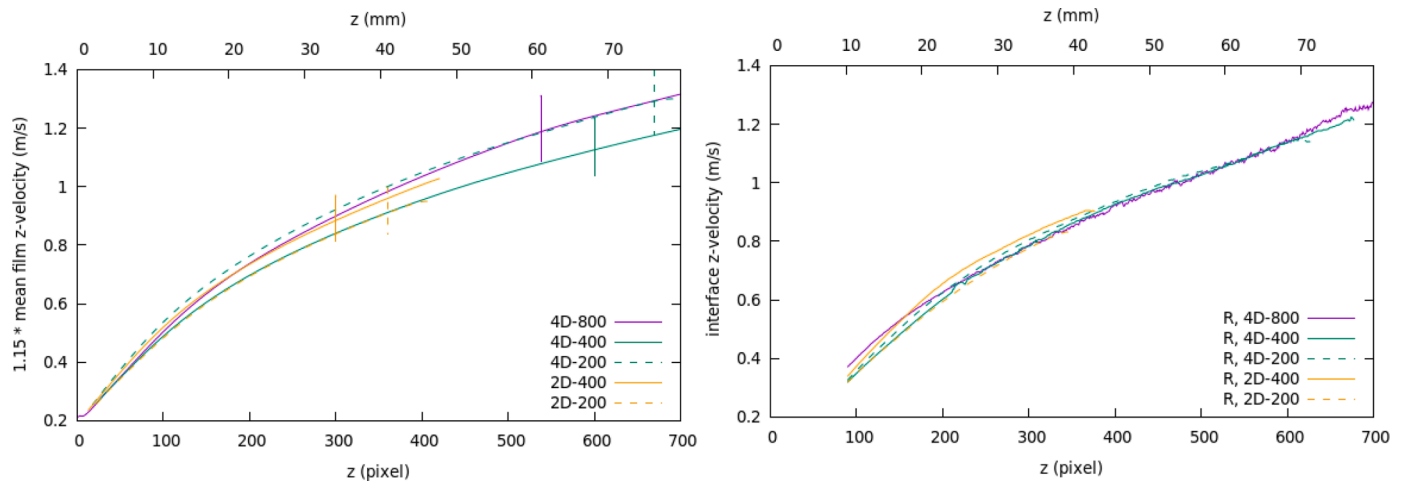


Fig. 9. Left: liquid film interface velocity profiles from film thickness measurements and continuity equation normalized to liquid mean velocity upstream of the bubble 0.18 m/s. Right: Interface velocities from disturbance wave propagation. Cross-correlation distance $H = 80$ pixels.

being swept down by the supercritical-like-flow by the liquid film as noted also by Fabre and Figueroa, 2014.

- 2) Capillary waves are assumed to be isotropically generated at the interface and therefore time averaging implicitly used in our cross-correlation analysis cancels the random disturbance wave directions. This makes the disturbance wave velocity equal to the time-averaged convective velocity of the water-air interface.

Of course, the random and isotropic nature of the disturbance waves is not self-evident. While we recognize the method of disturbance wave velocity measurements as a potential technique for direct measurement of the velocity of liquid-gas interface, we also plan further confirmation of our hypothesis with high fidelity simulations and PIV measurements.

Before we proceed to more detailed analyses of disturbance wave propagation, we need to comment certain deviations of the velocity profiles in Fig. 8 that demand additional comments of our measurements. Despite significant differences between the left- and right-side time averaged film thickness visible in inset graphs of Fig. 8, interface velocities predicted from the disturbance waves remain very similar on both sides. In all graphs of Fig. 8 one can actually see that the interface velocity is just slightly higher on the side of the photographs, where films are thinner for all five analyzed bubbles. The cases 2D-200 and 4D-400, where the difference between the left and right film thickness is larger, show slightly more pronounced, but still small differences between the left and right interface velocities. This tiny difference is estimated to be of the same order of magnitude as the uncertainty of the velocity profiles, however, since the same behavior was observed also in the measurements that are not presented in this Section (cases in Fig. 4), it might be real.

Further observations of Fig. 8 show that axial distance H between the points, where cross-correlations are computed, impacts the results of our measurements. The velocity profile with the largest discrepancy in Fig. 8 is the one obtained at distances $H = 40$ pixels and on the side with the very thin film of 4D-400 bubble. Just slightly lower discrepancies are observed for $H = 40$ pixel profiles in 2D-200 and 4D-200 bubbles. For sufficiently long H ($H = 80$ and 160 pixels) these differences are rather small. The first suspect for the discrepancies seen on curves for $H = 40$ pixels were the discrete time lags, which were even less than 1 frame at the highest velocities. If that was the main source of the discrepancies, it would be easily solved with higher camera frequencies. However, it has turned out that this was not the case; discrepancies at short H were observed also in measurements at 800 Hz and 1600 Hz camera frequencies, where time lags were several times higher. We have concluded that the main problem in the time-averaged disturbance velocity measurements in the region of the thin film lies in the spatial resolution of

the film, resolved on 2 to 5 pixels, and less in the low camera frequency. Very thin liquid film filters long wavelength disturbances, which are the most useful for cross-correlation based velocity measurements. Short wavelengths, which are emphasized on the thin films, are more difficult to resolve and correlate. The only solution is better spatial resolution of the photographs. Further analysis shows that even for short $H = 40$ pixels and low camera frequencies, where time lag is only about 1 frame, the interpolation still provides accurate results, as long as the liquid film is sufficiently thick to allow propagation of lower frequency and longer wavelength disturbance waves. This aspect of our analysis is further analyzed in the next Section 4.3 dedicated to frequency analyses.

Comparison of velocities obtained from direct measurements of film thickness and from disturbance waves are shown in Fig. 9 for the same experimental cases. Mean film velocities in the left image of Fig. 9 are multiplied with factor 1.15, which takes into account the difference between the maximum film velocity and the mean film velocity. The key message of Fig. 9 are uncertainties of the measurements: uncertainty of the velocities obtained from the film thickness measurements are clearly larger than the uncertainties of the velocity measurements from the disturbance waves. Direct quantification of the uncertainties of disturbance wave measurements is rather complex. Consequently, we estimate the uncertainties from Fig. 9 (right) to be predominantly stochastic, while the possible systematic errors that affect disturbance wave measurements are mainly due to the coordinate system fixed to the bubble nose point, which are similar for both types of our analyses.

4.3. Frequency analysis

Frequency analysis was performed with Fourier decomposition of the time dependent film thickness signals at each axial position along the pipe used for cross-correlation analyses. Frequency analysis and wave decomposition is especially efficient for linear systems or at least nearly linear systems. We can naturally expect, that wave decomposition is more successful for sufficiently thick films which allow propagation of lower frequency and larger wavelength disturbances. Thinner liquid films mean shorter wavelengths, higher frequencies, less precise interface detection, and possibly more pronounced nonlinear effects.

The first result of the spectral analysis are power spectra of the time signals at sufficiently large distance from the bubble nose. The length of the time signals used in power spectra computations was slightly modified: 49,152 points out of 49,778 were used as six independent samples of $8192 = 2^{13}$ points. Spectra of each sample were computed and six samples were averaged after that. With this approach, we have avoided very large oscillations in the spectra of a single long signal.

Typical power spectra of film thickness time signal observed at a

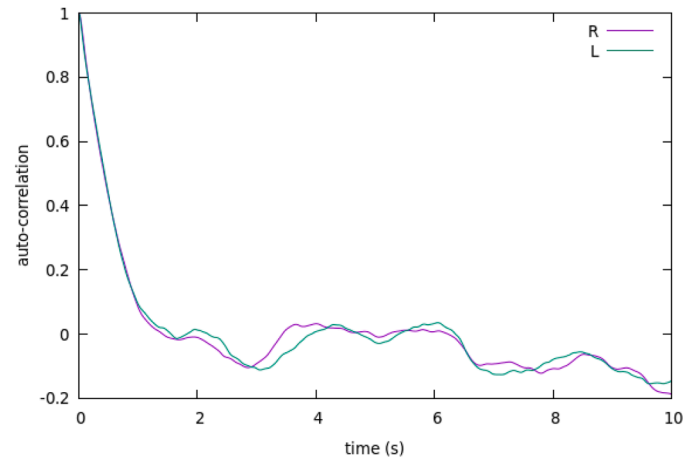
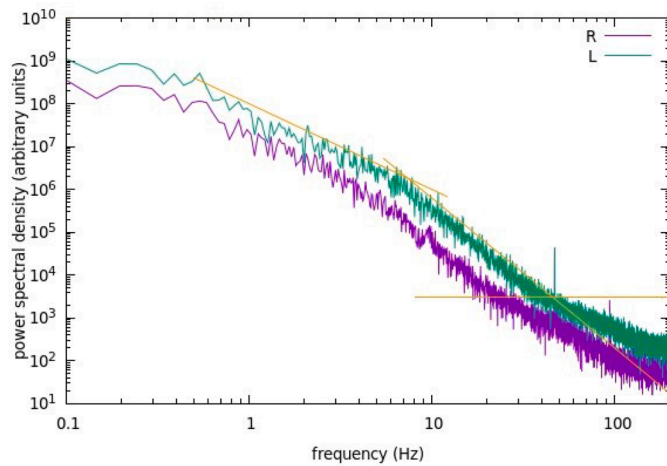


Fig. 10. Left and right side power spectra (left) and corresponding auto-correlation functions (right) of 4D-400 case at axial position $z = 500$ pixels downstream the bubble nose. Both obtained as average of six samples of 20 s (8192 points) each. Yellow curves: x^{-2} , $x^{-3.5}$, $x = 3000$.

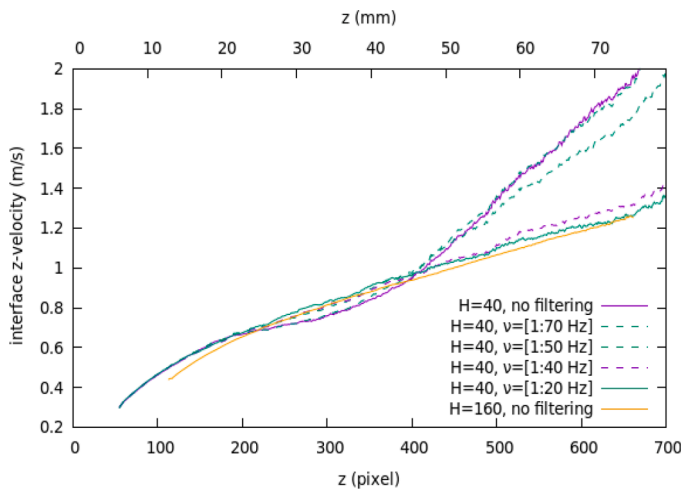


Fig. 11. Frequency space filtering of Taylor bubble 4D-400 thin side film. Legend: frequencies retained in the spectrum of the time signals.

fixed distance $z = 200$ pixels from the bubble nose point are shown in the left image of Fig. 10. Spectrum is computed as square of the Fourier transformation of film thickness signal, which is equivalent to the Fourier transformation of the autocorrelation function of the signal shown in Fig. 10, right. Two spectra and two auto-correlation functions in Fig. 10 are given for 4D-400 case left and right film thickness signals. These spectra are representative also for spectra at other axial locations with well-developed liquid film at distances larger than $D/2$ (100 pixels) from the bubble nose, and for spectra of the other experimental cases. The only visible difference between spectra of the other bubbles would be difference between the left- and the right-side spectra, which is more pronounced for cases with larger differences in liquid film thickness.

The shape of the power spectra can be discussed in comparison with typical frequencies of the liquid turbulence in the pipe above the bubble, which is assumed to be one of the key sources of the interfacial waves. The frequencies below approximately 1 Hz stem from the frequencies of the large scale turbulent vortices and at the same time correspond to the manual manipulations of the bypass valve used to compensate the turbulence and to regulate the flow rate through the section. From the DNS database of Kasagi (Fukata and Kasagi, 2002), pipe flow case at $Re = 5300$, which is close to our experimental conditions, we have obtained typical frequencies of the smallest turbulent structures in such flow. The highest frequencies obtained from Kolmogorov length and time scales

are between 10 Hz and 70 Hz in the axis of the pipe and in the near-wall region, respectively. Since most of the turbulent kinetic energy at the Kolmogorov scales is already dissipated, the lower frequencies between 3 and 20 Hz, which correspond to the Taylor microscales, seem to be more relevant as the upper limit. Consequently, the main excitations of the Taylor bubble are expected at frequencies below 20 Hz. The frequencies that follow from the theory are in rough agreement with our measurements. The power spectral density graph in Fig. 10 roughly follows the x^{-2} slope at frequencies between 0.5 and ~ 5 Hz and the slope around $x^{-3.5}$ at frequencies from ~ 10 Hz to ~ 40 Hz, which points to a rapid dissipation in this region. The power spectral density above 40 Hz already drops for around six orders of magnitude and must be ignored due to the numerical errors from interface reconstruction and possible external noise below the line around $x = 3000$. Very similar spectra, with the same characteristics are observed also at the other locations and in the other experimental cases.

The frequencies below 1 Hz have the strongest impact on the auto-correlation function in Fig. 10, where several oscillations, going above and below zero, are observed on a scale of a couple of seconds, but without a clear order. Similar auto-correlation functions with irregular oscillating behavior at times above 1 s are observed also for other experimental cases.

Further Fourier analysis is based on Fourier transformations of time signals at all axial distances along the bubble length. Different frequency bands can be removed in the frequency space and after that the signals are transformed back into the time domain. These filtered time signals are used to compute the cross-correlation coefficients in exactly the same way as explained in Section 4.1. Shorter time signals of $32768 = 2^{15}$ points, out of total 49,778 frames, were used to speed up the Fourier transformations.

The focus of our Fourier analysis is on the thin side film of the 4D-400 bubble, where the largest discrepancies were observed between disturbance wave velocities obtained at different cross-correlation distances H in Fig. 8. Filtering of the low frequencies from the lowest of around 0.01 Hz and up to 1 Hz, did not affect the disturbance wave velocity profiles. Frequencies above 70 Hz are also irrelevant, which is somehow clear from the results shown in previous sections, where we claim that sufficiently accurate results are obtained at camera frequencies 200 Hz and 400 Hz, which can capture 100 Hz and 200 Hz frequency waves, respectively. Consequently, the curve 'H = 40, $\nu = [1:70$ Hz]' in Fig. 13, which denotes filtering of the frequencies below 1 Hz and above 70 Hz, remains almost unchanged in comparison with the original profile obtained with no filtering at cross-correlation distance $H = 40$ pixels. Waves of frequencies between 1 and 40 Hz are found to deliver the largest amount of information for disturbance wave velocities studied in

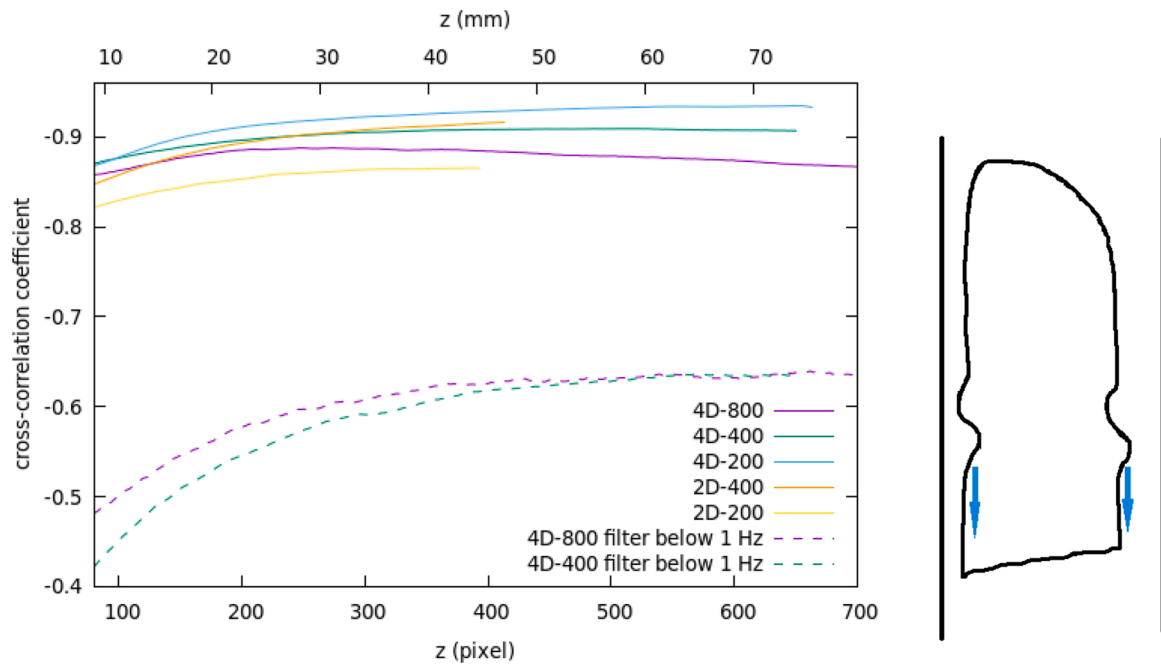


Fig. 12. Cross-correlation of film thickness time signals between the left and the right points at the same axial distance for bubbles in Fig. 7. Solid lines: time signals without frequency filtering, dashed lines: frequencies below 1 Hz removed from the signals. Right drawing: correlated disturbance waves.

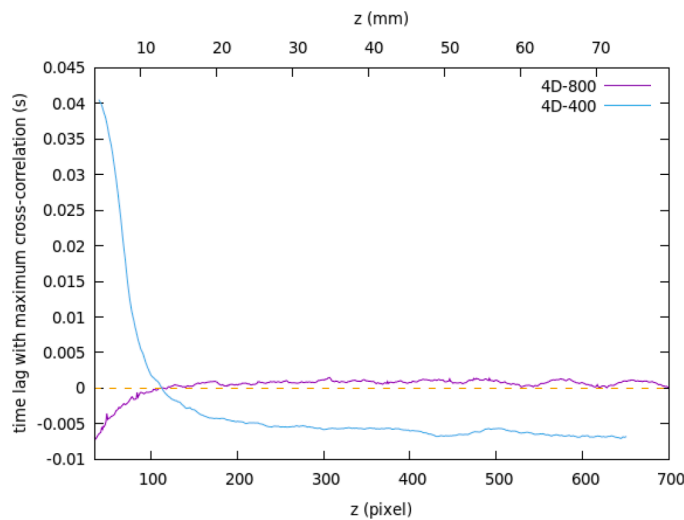


Fig. 13. Optimal time lag between time signals at the left and right points at the same axial position that results in the most negative cross-correlation coefficient of both signals.

our work. The problematic frequency band, which is responsible for the discrepancies of the disturbance velocity measurements in Fig. 8 at cross-correlation distance $H = 40$ pixels, is above 40 Hz. As shown in Fig. 11, cutting out the frequencies above 40 Hz results in coherent disturbance velocity profiles predictions at all cross-correlation distances H . Another profile ' $H = 40, \nu = [1:20 \text{ Hz}]$ ' in Fig. 13 shows that the waves in the range of 1 Hz – 20 Hz are crucial and should not be filtered from our signals.

Similar analyses were performed on the other side of the same bubble and on the other bubbles, where the filtering was found to be less beneficial in comparison with the case 4D-400, where the influence of the frequency filtering is the most obvious. Similar filtering of the frequencies above 40 Hz applied for other experimental cases is not shown, but gives only minor improvement in the agreement of the profiles

obtained at $H = 40$ pixels, and practically no changes at higher H 's. Consequently, we see the filtering in frequency space as a potential tool for refinement of the measured results. However, filtering itself cannot compensate deficiencies in spatial and temporal resolution of the measurements.

4.4. Cross-correlation of left- and right-side disturbance waves

Another subtle detail can be seen from Fig. 6 showing temporal development of liquid film thickness in several points on both sides of the Taylor bubble: both films seem to be in negative cross-correlation. Fig. 12 shows values of cross-correlation coefficients computed between the film thickness time signals on both sides of the photographs at each axial distance downstream the bubble. Rather strong negative cross-correlation coefficient means that the disturbance waves travelling downstream the Taylor bubble behave like a wobbling of the whole Taylor bubble body from one side to the other side of the walls (sketch in Fig. 12, right). Knowing the wave behavior on one side of the Taylor bubble tells a lot about the film on the other side. One can imagine this as a translatory motion, which first moves the nose of the bubble in the direction perpendicular to the pipe axis, and the rest of the bubble follows the translation with a traveling wave.

The observation of the correlated waves on both sides of the photographs of the various Taylor bubbles gives a hint about the possible source of the disturbance waves: it looks that the most of the waves are being produced somewhere at the bubble nose position by the instability of the bubble nose or the liquid turbulence structures that hit the bubble nose.

Filtering of frequencies below 1 Hz was found to affect the cross-correlation of film thickness time signals between the left and the right points at the same axial distance for bubbles shown in Fig. 12. For the specific case of 4D-400 Taylor bubble, the cross-correlation coefficient with a plateau at -0.9 value, drops to around -0.6 (dashed lines in Fig. 12), when the lowest frequencies below 1 Hz are eliminated. This result identifies the low frequency oscillations introduced by the large scale turbulence and manual manipulations of the flow rate as the most important generators of the disturbances that produce coherent disturbance waves on both side of the Taylor bubble. We must stress that this

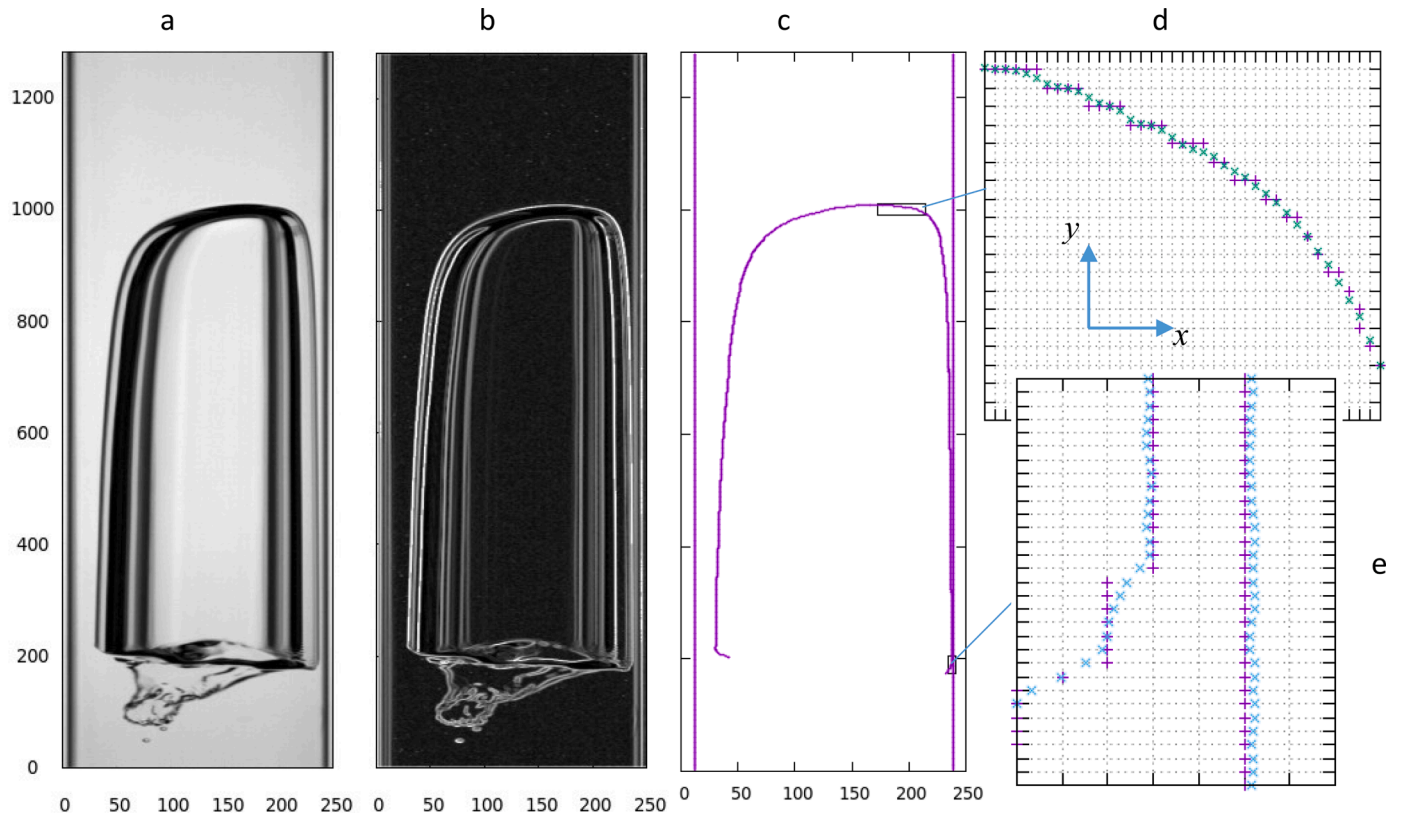


Fig. 14. Left to right: a) original image, b) magnitude of the gradients field (step 1), c) extracted bubble interface and pipe inner walls at pixel level (step 2), d, e) refinement of the interface position at subpixel level (step 3) with pixel grid in the background: violet "+" - pixel level interface, blue and green "x" - sub-pixel level interface. All units in pixels. Scales on x and y axes are not in proportions.

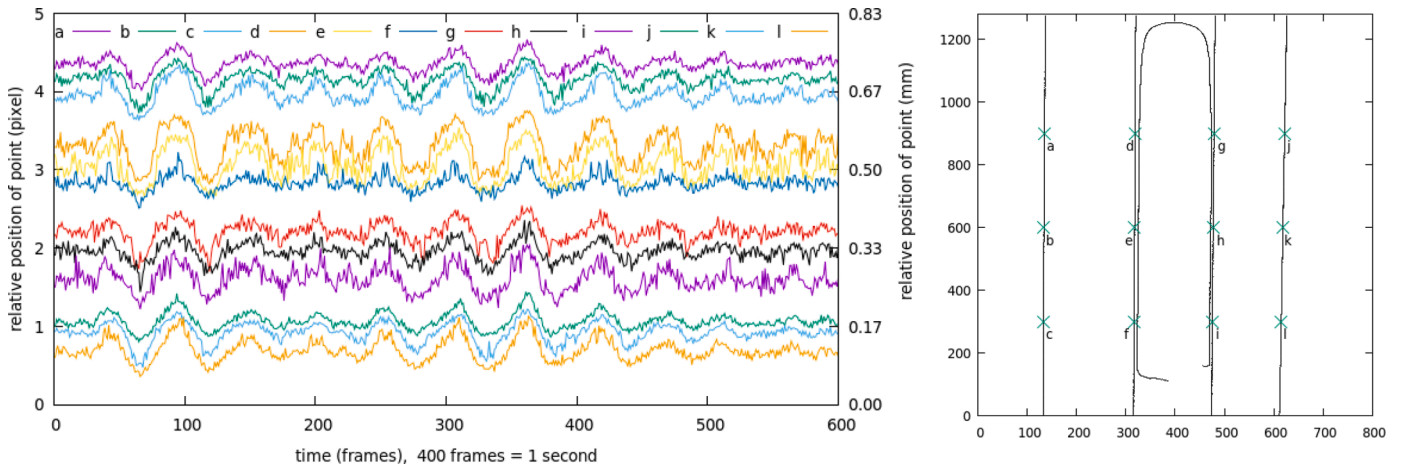


Fig. 15. Oscillations of the 6 points on the outer wall of the rectangular water tank (points a, b, c, j, k, l in right drawing), and the 6 points on the inner side of the glass pipe (points d, e, f, g, h, i). Profiles are arbitrarily shifted in the y direction. Right image: positions of the analyzed points in pixel scale.

coherence was not visible directly from the videos due to the very small amplitudes of the disturbance waves.

An additional piece of information on the source of the disturbance waves can be obtained by cross-correlation of the film thickness time signals on both sides, where a film thickness at particular axial position on the right side of the photographs is correlated with film thickness at the same axial position on the left side of the film, but with variable time lag between both signals that results in the most negative cross-correlation coefficient. Maximum anti-correlation at a non-zero time-lag means that the signal on one side of the bubble travels faster than on the other side. Only axial velocity of the disturbance waves is revealed

with this approach. Fig. 13 shows time lags resulting in maximum cross-correlation of time signals in the points at the same axial distances on the left and right side of the bubble. An ideal axisymmetric bubble with symmetric velocity field and with the disturbance waves generated exactly at the nose point and traveling at the precisely the same speed, would show maximum anti-correlation for zero time lag. Two curves in Fig. 13 are given for the cases 4D-400 and 4D-800 in Fig. 5, where the time averaged position of both bubbles is given: thinner liquid film appears on the right of the 4D-400 bubble, and on the left side of the 4D-800 bubble. Positive time lag means that the signal on the left side travels faster than the signal on the right side. For the 4D-400 case,

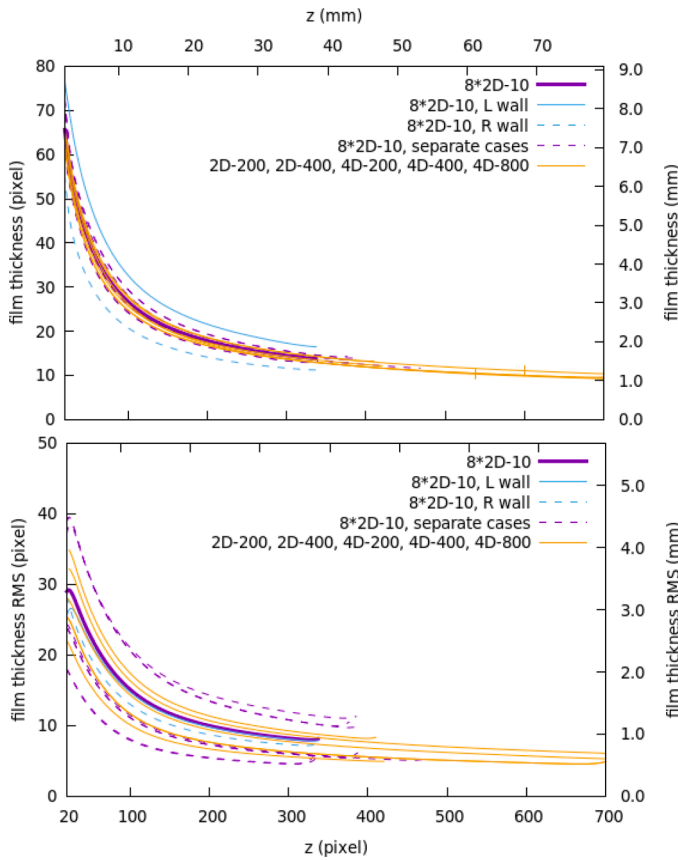


Fig. 16. Top: Average film thickness of 13 bubbles analyzed in the present study. Measurement uncertainty (not plotted) is below 1 pixel (0.1 mm). Bottom: RMS fluctuations of the averaged interfaces.

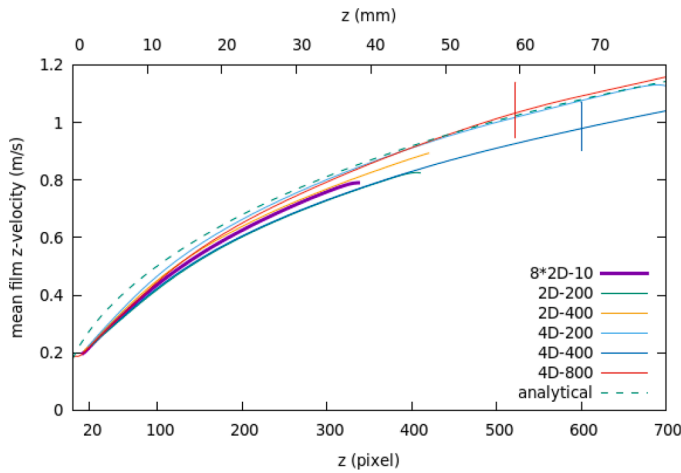


Fig. 17. Mean downward film velocity (m/s) based on film thickness measurements and continuity equation.

disturbance waves travel faster on the side of the thick liquid film for approximately the first 100 pixels of axial distance. The left-side waves catch their right-side counterparts at around 120 pixels and overtake them on the remaining length of the bubble. Similar, but less pronounced phenomena is seen in the 4D-800 case: axial velocity of waves along the thick side of the film is higher at the nose of the bubble, but slightly slower after approximately 100 pixel downstream distance. This result suggests, that the sources of disturbance waves act roughly at the axis of the pipe, where the bulk liquid flow hits the bubble nose.

The accuracy of the analysis shown in Fig. 13 is not particularly large, because computation of the most negative cross-correlation coefficient at various time lags is not very well posed: cross-correlation coefficients of around -0.9 at zero time lags in Fig. 12 are just slightly larger at optimal non-zero time lags in Fig. 13. However, qualitatively similar behavior is observed also for bubbles not shown in Fig. 13. With the existing techniques we cannot precisely quantify the actual difference in velocities on both sides of the film. At distances more than half of pipe diameter (~100 pixels) downstream from the bubble nose, we can only roughly compare the time lags between 1 and 5 ms in Fig. 13 with the 100 ms time interval needed by the disturbance wave to travel along the 4D bubble length. This ratio, around 1% to 5%, is also a rough difference between the thin and thick liquid film interface velocity. The conclusion of Section 4.4 is in agreement with the Fig. 8 results: we observe slightly faster disturbance wave velocities on the side with a thinner liquid film. However, precise quantification of the velocity difference will require more accurate measurements.

4.5. Limitations of the disturbance wave tracking method

One of the "holy grails" of two-phase flow measurements is measurement of instantaneous interface velocities. It is clear that our disturbance wave based technique cannot provide instantaneous values, neither in time nor in space. Results in the previous sections were obtained from measurements recorded over at least 1 min interval at 800 Hz frequency. Thus, we have attempted to measure disturbance wave velocities on shorter time intervals, which would reduce the time averaging effect of the measurements. The time lags were computed at distance $H = 80$ pixels and for time signals of 10 s duration. The time interval of 10 s is roughly 10 times shorter than the 80 s time interval of the 4D-400 recording used in frequency analyses, and at the same time roughly 50 times longer than the flow-through time of the liquid film past the Taylor bubble of 4D length. Many independent disturbance waves are expected to be generated during that time and the cross-correlations are expected to generate similar results as on longer time intervals of 80 s. Most of the velocity profiles obtained from 10 s time intervals are indeed very similar to the velocity measured over 80 s. However, some of the 10 s intervals, roughly 1 out of 10, show significant difference. The disturbance wave velocity predicted on such particular time interval is significantly higher than the velocities of other profiles. Detailed examination of the cross-correlation coefficients on such time interval shows that they are much more blurred and that extraction of the maximum correlation from these curves is poorly conditioned in comparison with the other time intervals with "normal" behavior. Consequently, measurement of the disturbance wave velocity on this interval cannot be trusted. When we look at the Taylor bubble behavior on the problematic time interval, we can observe that the bubble significantly changed its radial position in a very short time interval below 0.1 s. Further tests performed with measurements of disturbance wave velocities on even shorter time intervals, have shown amplified behavior of failed predictions of reconstructed disturbance waves in comparison with 10 s time intervals. We can eventually conclude, that applied spatial resolution and the current status of our interface recognition software do not allow accurate velocity measurements on time intervals shorter than roughly half a minute.

5. Conclusions

Present study focuses on the dynamics of a smooth interface region of the Taylor bubble in a vertical turbulent counter-current air-water flow, disregarding the phenomena of the bubble's tail region. The dynamics of the smooth interface region contains a wealth of phenomena, which were identified, explained, and more or less successfully quantified.

The first step into the present study was the development of the in-house computer codes that converted digital photographs of Taylor bubbles in a glass pipe into two-dimensional silhouettes of Taylor

bubbles with absolute precision of around 1 pixel and approximately five times lower relative uncertainty. Processing of large amounts of data, 50000 photographs per experimental case, left very small amount of space for manual corrections of the failed interface reconstructions. The photographs or segments of photographs with failed spatial reconstruction of the interface were eventually corrected with temporal interpolation.

The main goal and motivation of the research was to obtain a time averaged shape of the Taylor bubble interface. We have shown that this goal cannot be achieved accurately with time averaging of two-dimensional silhouettes alone. Namely, the unstable nature of the bubble in counter-current flow turned out to be "quasi-stable". We have observed that eccentric position of the bubble's nose, which was randomly taken by the bubble during the initial transient of the air injection, remained unchanged for several minutes of the particular experimental case. Initial azimuthal positions of the Taylor bubbles were found to be stochastic. Averaged bubble shape, which included azimuthal direction averaging, was eventually obtained with ensemble averaging of several time averaged cases, however, the uncertainties remained large; probably too large for comparison with similar experiments or with accurate simulations. We believe that the final shape of the time averaged bubble, which would retain the axial asymmetry, should be eventually obtained with three-dimensional imaging.

The second part of this study was enabled by the high relative accuracy of our interface reconstruction technique, which was found to be almost an order of magnitude more accurate than the absolute accuracy of the interface reconstruction. The key result of this analysis is a method based on cross-correlation of film thickness temporal development measured at different axial locations of the bubble. The method predicts velocities of the disturbance waves traveling over the Taylor bubble's body. All additional analyses, including those based on spectral decomposition of the time signals, indicate that the disturbance wave velocity measured over sufficiently long interval of several dozen seconds, becomes equal to the axial water-air interface velocity. The main contributors to the cross-correlation measurements are low frequency and low celerity waves, which are slow in comparison with the interface velocity. Consequently, tracking of these waves appears to offer a technique for measurements of the time averaged interface velocity.

Using the method of disturbance wave tracking, we have shown that the waves on the Taylor bubble interface are mainly generated near the axis of the pipe and travel from the bubble nose downstream in a way that is similar to the snake motion of the bubble. Interface velocity seems to be slightly higher on the side with thinner liquid film than on the thicker film side. Although the precise quantification of the tiny velocity difference was not possible, this result is somehow expected: according to the Bernoulli equation, slightly lower velocity of the thicker film

means higher local pressure that is pushing the Taylor bubble towards the side with the thinner film.

Independent validation of the results of this paper with high fidelity LES+VOF simulations of the Taylor bubble in the configuration of our experiments is a work in progress. Possible improvements of the existing experiment and data processing will be focused on cross-correlations on short time scales and finer resolution videos, which will capture only a part of the Taylor bubble. Another test of our hypothesis on equality of interface velocity and interface disturbance waves is expected also from the combination of captured videos with PIV analyses of liquid velocity fields.

Data availability

Data (Taylor bubble videos) and computer codes used for image processing and data analyses are available from the corresponding author upon reasonable request.

CRediT authorship contribution statement

Jan Kren: Conceptualization, Data curation, Formal analysis, Investigation, Methodology, Software, Visualization, Writing – original draft. **Boštjan Zajec:** Conceptualization, Data curation, Formal analysis. **Iztok Tiselj:** Conceptualization, Data curation, Formal analysis, Writing – original draft, Resources, Software, Visualization. **Samir El Shawish:** Conceptualization, Formal analysis, Writing – review & editing. **Ziga Perne:** Investigation. **Matej Tekavčič:** Methodology, Validation, Resources, Writing – original draft. **Blaž Mikuz:** Conceptualization, Investigation, Resources, Writing – review & editing.

Declaration of Competing Interest

The authors declare that they have no known competing financial interests or personal relationships that could have appeared to influence the work reported in this paper.

Data availability

Data will be made available on request.

Acknowledgements

The authors gratefully acknowledge financial support provided by Slovenian Research Agency, grants P2-0026 and NC-0026.

Supplementary materials

Supplementary material associated with this article can be found, in the online version, at [doi:10.1016/j.ijmultiphaseflow.2023.104482](https://doi.org/10.1016/j.ijmultiphaseflow.2023.104482).

Appendix A – Image Processing

Roughly 50000 photographs taken in each experiment were processed by the newly developed in-house software that has relied on widely used libraries for fitting of the two-dimensional surfaces and one-dimensional lines, Fourier transformations, and cross-correlation of one-dimensional functions collected in the Numerical Recipes book (Press et al. 2007). The key part of these computer codes was image processing that resulted in extraction of the Taylor bubble surface from the images. We have followed rather standard image processing methods that can be found in open literature. Our rough guide was a document of Grishchenko (2011), which was prepared within the scope of our joint project with the authors of the report in 2011. Since the image analysis is being applied on large number of photographs, we have a very limited possibilities for manual corrections of the photographs and possible artefacts. Thus, a robust procedure was needed, which reported possible failures in bubble interface reconstruction. A rough description of the algorithm is given below and the main intermediate results and final results of reconstruction are shown in Fig. 14:

1 Convert image intensity matrix into gradient matrix

The original digital photograph and video (Fig. 14a) has intensities given as a matrix of integers. This matrix is converted into a field of gradients. The gradient was calculated on a staggered grid, where the four closest points were used for the calculation. The magnitude of the gradient field is shown in Fig. 14b.

1 Identification of Taylor bubble outer surface

The most demanding step of the algorithm was identification of the Taylor bubble outer surface and its extraction. The problem of this step is obvious from Fig. 14b: the image of Taylor bubble contains several curves that are a consequence of the various light reflections in the system. The outer surface of the bubble, which gives the extent of the bubble at the pipe cross-section perpendicular to the camera direction of view, is very seldom the curve with the largest magnitude of the gradient. The subroutine responsible for identification of the outer surface shown in Fig. 14c is divided into two steps:

- 1.%2 **Identification of the bubble nose** finds the most exposed point (point=pixel) on the top of the bubble. By approaching the bubble from the top, the point with sufficiently large gradient is identified as the nose of the bubble. On most images, this is a rather trivial task, which often relies on the position of the nose on the photograph taken in the previous time step. Problems that need to be avoided in advance for smooth performance of this subroutine are minor bubbles of around millimeter size that can arrive with the incoming water flow and can be falsely recognized near the actual Taylor bubble nose.
- 2.%2 **Outer surface identification.** After the bubble nose point is found, a new subroutine is called, where the neighboring points are examined and the continuation of the interface curve is sought. The neighboring point with sufficiently strong magnitude of gradient is selected, if the direction of the gradient in this point is not far from the direction of the gradient vector in the previously recognized surface point. The new point is not necessarily the point with the largest gradient among the neighbors - this choice would shift the interface recognition from the outer surface to the reflections seen inside the bubble (Fig. 14b), which can contain stronger gradients than the bubble surface. The procedure is called twice: first, the variation of the gradient direction is sought in clock-wise direction from the bubble nose point, and then in the other direction. The iterative search of the neighboring points on the surface is stopped after the difference between the angle of the gradient vector in the most recently identified point on the surface and the gradient direction in the bubble nose point is larger than prescribed value (typically between $\pi/2$ and π).

1 Sub-pixel Interface position refinement

When the surface of the Taylor bubble cap and body is identified and the result shown in Fig. 14c is obtained, the algorithm of the interface position refinement is applied. At each pixel, where the surface was identified in the step 2, the surface position is refined through the detailed analysis of the local gradient around this point. Magnitudes of the gradients are considered on 5×5 grid points around each relevant pixel. Surface of gradient magnitude is fitted using 6-parameters quadratic equation of two variables on the observed Cartesian 5×5 grid. The best fit is required in the relevant pixel, slightly weaker fit in the first neighbors, and the weakest fit is required in the points on the edge of the 5×5 grid. Maximum values of the gradient magnitude are sought on the fitted surface with imposed constraints: local maxima must lie on the discrete lines that cross the grid formed by the pixels. For example: if the subgrid refinement is sought around the pixel (i, j) at coordinates (x_i, y_j) , the refined position of the maximum gradient magnitude must lie either on the $x_i = \text{const}$ or $y_j = \text{const}$ lines as shown in Figs. 14d and e. The maximum gradient is accepted as a point on the interface, if the local curvature of the fitted surface is sufficiently large and the point lies less than ~ 0.7 pixels from the position of the starting pixel (x_i, y_j) . Example of the interface after subgrid refinement is shown in Fig. 14d and Fig. 14e. Green and blue crosses in Figs. 14d and e show subgrid refined interface points on lines $x_i = \text{const}$ and $y_j = \text{const}$ lines, respectively.

A simpler version of line reconstruction algorithm was applied for extraction of the inner walls of the glass pipe. The basic algorithm described above, did not perform with desired precision due to the thick gradient region, which was always present on one side of the pipe. In the case of Fig. 14a, the non-sharp gradient is present on the left wall. It has been verified in a separate test with an immersed object that the wall position corresponds to the position of a very weak gradient. Consequently, the wall recognition algorithm recognized the wall at the position of the minimum light intensity of the original image Fig. 14a (not gradient), and later corrected the wall position for an appropriate visually determined distance towards the axis of the pipe. The reconstruction is based on a smaller 3×1 stencil of cells in step 3 of the algorithm, where only two neighbors in wall normal direction are used to determine the position of the wall.

A.1. Accuracy of the interface reconstruction

The image processing algorithm briefly sketched above and the results of the processing shown in Figs. 14d and e, represent the starting points for the analyses of the interface dynamics presented in the Sections 3 and 4.

A couple of remarks are needed at the end of the Section on image processing. Quality of the sub-pixel resolution was verified (rather accidentally) with tiny oscillations of the whole test section observed in some of the measurements, which later evolved into the "shake-the-section" test. In-phase oscillations with an amplitude of around one quarter of the pixel (around 50 micrometers) were observed in various points of the section shown in Fig. 15. This analysis was performed on a short time interval of 1.5 s and 600 photographs. The main frequency of around 8 Hz, which can be recognized in Fig. 15, is close to the estimated natural frequency of the test section of around 10 Hz. The amplitudes in all points are giving a good clue about the relative error of the sub-pixel interface reconstruction technique, which is estimated to be between one tenth and one quarter of the pixel. The image reconstruction displayed in Fig. 15 exhibited a high level of sensitivity, enabling us to detect structural vibrations. Therefore, we refrained from applying a common image analysis method that involves eliminating the background image without the Taylor bubble in our analyses, as this procedure would eliminate the structural vibrations. Ignoring structural vibrations was recognized as detrimental for our analyses presented in Section 4.

A.2. Interface reconstruction failures

The step 2 of the algorithm for interface reconstruction fails on three occasions, which usually result in a global reconstruction failure, where a complete Taylor bubble interface or large sections of the bubble interface remain unidentified:

- i) When the bubble nose is not correctly identified by the subroutine described in the step 2.1.
- ii) When the liquid film thickness between the bubble and the glass wall falls below 2 – 5 pixels, and gradient magnitudes of the bubble interface interferes with the pipe wall gradient (step 2.2), and
- iii) when the two-nose bubble appears. This case is extremely rare (below 1 out of 50,000 photographs).

Missing data from the global reconstruction failures are acceptable for the further analyses of the bubble behavior, as long as the number of these failures remains low. In numbers: our software fails to recognize large sections of the bubble interface at resolution 9 pixels per millimeter in roughly 1 out of 10,000 photographs.

Failures of the sub-pixel refinement step 3 in our algorithm result in missing positions of the interface in some points. Missing sub-pixel points are more likely to appear in the thin liquid film, an example is shown in Fig. 14e, which is around 2 pixels wide in that region. In quantitative terms: for thin film of thickness 2 to 5 pixels, we observe up to around 500 failed reconstructions in 50,000 photographs in each particular axial or radial location. Number of failed local reconstructions falls to around hundred for a film thickness of around 10 pixels.

Further analyses of the photographs eliminated the interface recognition failures with interpolations that were performed in time and in space to fill all large failures mentioned in step 2 and local failures in sub-pixel reconstruction in step 3. As seen in the Sections 3 and 4, the failures in the interface reconstruction reduced the accuracy of our analysis, but did not prevent it.

Appendix B - Time averaged liquid film thickness and mean velocity of the liquid film

The asymmetry of the time averaged Taylor bubble shown in Figs. 4 and 5 is problematic for independent verifications of our measurement. However, by averaging both sides of our silhouettes we are able to obtain results that are less sensitive to the asymmetry. These results are presented in Fig. 16, which shows liquid film thickness along the bubble, where time and ensemble averaging are combined with the left-right side averaging of our photographs.

Axial distances on x-axis of Fig. 16 are measured from the bubble nose. Thick violet profile is the time + ensemble + left-right averaged profile of the measurements from the Figs. 4 and 5. Two blue lines, which represent the envelopes of all other curves, are time and ensemble averaged profiles of the Fig. 4 cases, but for the left and for the right side separately. It is clear that all eight left-right averaged dashed violet curves for each measurement in Fig. 4 and additional five orange curves of the measurements shown in Fig. 5, fit inside the envelopes.

While the combined time + ensemble + left-right averaging result in reasonably narrow definition of the liquid film thickness, the RMS dispersion of the film thickness remains high, as shown in the bottom graph of Fig. 16. The left-right averaging, which narrows the film thickness, is increasing the RMS dispersion of the film thickness. This is an expected results in asymmetric bubble shape, where film on one side is below the average film thickness most of the time, while the film on the other side is thicker.

Typical variation of different time-averaged liquid film thickness in the top drawing of Fig. 16 is estimated to around 1 pixel at distances more than one pipe diameter D (~ 200 pixels) from the bubble nose and around 2 pixels at lower distances. Absolute uncertainty of time-averaged film thickness is also around 1 pixel, which amounts to 10% relative error at axial distances more than 200 pixels from the bubble nose. Uncertainty of the curves in the axial direction, as a consequence of the uncertainty in the bubble nose location, is also estimated to around 1 pixel, however, this is a minor contribution to the film thickness uncertainty.

Another simple curve can be obtained from the measured and averaged film thickness profiles: for known upstream liquid velocity, a mean downward liquid velocity in the film can be obtained from the continuity equation as $v(z) = v_0 R^2 / [2Rh(z) - h(z)^2]$, with the pipe radius $R = 13$ mm, upstream fluid velocity ahead of the bubble $v_0 = 0.18$ m/s, and liquid film thickness $h(z)$. These profiles are shown in Fig. 16 separately for time, ensemble and left-right averaged film of eight measurements from Fig. 4 and separately for five measurements from Fig. 5. The velocity profiles computed from the continuity equation shown in Fig. 17 are strictly valid only for the bubble of circular cross-section. This condition is relatively well satisfied: time development of the Taylor bubble diameter, computed from the liquid film thickness measured on photographs, has shown variations of $\pm 2\%$ or less measured at axial locations of one pipe diameter or more downstream from the bubble nose. Consequently, we consider the time averaged film thickness as a relatively accurate measure of the bubble diameter, which is applicable also for the evaluation of the mean velocity in the liquid film. Accordingly, the relative uncertainty of the time averaged mean film velocity profiles is of similar size as the uncertainty of the mean film thickness measurements: around 10% at distance larger than D from the bubble nose.

Dashed curve in Fig. 17 marked as "analytical" is an approximate solution of the simplified film momentum equation that considers the film near the Taylor bubble as a free-falling film under the force of gravity, which is opposed by the wall shear stress force. Shear of the air in the bubble is neglected. An approximate analytical curve is a numerical solution of the model:

$$\frac{dv(t)}{dt} = g - \frac{f_w v(t)^3}{4Rv_0}, \quad \frac{ds(t)}{dt} = v(t)$$

with s denoting the axial position of the mass point in the film, $R=13$ mm, the bulk liquid velocity above the bubble $v_0=0.18$ m/s, and friction factor $f_w(\text{Re}_{\text{film}} = 12000) = 0.025$ (Moody, 1944). The observed agreement between the measurements and the profile obtained from the simple analytical model indicates that shear of the air flow inside the bubble is indeed very low and air-liquid velocity coupling over the bubble interface is rather weak.

References

- Abubakar, H., Matar, O., 2022. Linear stability analysis of Taylor bubble motion in downward flowing liquids in vertical tubes. *J. Fluid Mech.* 941, A2. <https://doi.org/10.1017/jfm.2022.261>.
- Alekseenko, S.V., Cherdantsev, A.V., Heinz, O.M., Kharlamov, S.M., Markovich, D.M., 2014. Analysis of spatial and temporal evolution of disturbance waves and ripples in annular gas-liquid flow. *Int. J. Multiphase Flow* 67, 122–134. <https://doi.org/10.1016/j.ijmultiphaseflow.2014.07.009>.
- Araújo, J.D.P., Miranda, J.M., Pinto, A.M.F.R., Campos, J.B.L.M., 2012. Wide-ranging survey on the laminar flow of individual Taylor bubbles rising through stagnant Newtonian liquids. *Int. J. Multiphase Flow* 43, 131–148. <https://doi.org/10.1016/j.ijmultiphaseflow.2012.03.007>.
- Ayati, A.A., Farias, P.S.C., Azevedo, L.F.A., de Paula, I.B., 2017. Characterization of linear interfacial waves in a turbulent gas-liquid pipe flow. *Phys. Fluids* 29 (6), 062106. <https://doi.org/10.1063/1.4985717>.
- Benattallah, Aloui, Souhar, 2011. Experimental analysis on the counter-current Dumitrescu-Taylor bubble flow in a smooth vertical conduct of small diameter. *JAFM* 4. <https://doi.org/10.36884/jafm.4.04.11940>.
- Bergant, R., Tiselj, I., 2007. Near-wall passive scalar transport at high Prandtl numbers. *Phys. Fluids* 19, 065105.
- Cerqueira, R.F.L., Paladino, E.E., 2020. Experimental study of the flow structure around Taylor bubbles in the presence of dispersed bubbles. *Int. J. Multiphase Flow* 133, 103450. <https://doi.org/10.1016/j.ijmultiphaseflow.2020.103450>.
- Cerqueira, R.F.L., Paladino, E.E., Evrard, F., Denner, F., Wachem, B., 2021. Multiscale modeling and validation of the flow around Taylor bubbles surrounded with small dispersed bubbles using a coupled VOF-DBM approach. *Int. J. Multiphase Flow* 141, 103673. <https://doi.org/10.1016/j.ijmultiphaseflow.2021.103673>.
- Coste, P., 2013. A large interface model for two-phase CFD. *Nucl. Eng. Des.* 255, 38–50. <https://doi.org/10.1016/j.nucengdes.2012.10.008>.
- Davies, R.M., Taylor Geoffrey Ingram, 1950. The mechanics of large bubbles rising through extended liquids and through liquids in tubes. *Proc. R. Soc. Lond. B Biol Sci.* A200375–390. <http://doi.org/10.1098/rspa.1950.0023>.
- Delfos, R., Wisse, C.J., Oliemans, R.V.A., 2001. Measurement of air-entrainment from a stationary Taylor bubble in a vertical tube. *Int. J. Multiphase Flow* 27, 1769–1787. [https://doi.org/10.1016/S0301-9322\(01\)00029-5](https://doi.org/10.1016/S0301-9322(01)00029-5).
- Delfos, R., Rops, C.M., Kockx, J.P., Nieuwstadt, F.T.M., 2001. Measurement of the re-coalescence flux into the rear of a Taylor bubble. *Phys. Fluids* 13, 1141–1150. <https://doi.org/10.1063/1.1360713>.
- De Moura, B.F., Martins, M.F., Sepúlveda Palma, F.H., Da Silva, W.B., Cabello, J.A., Ramos, R., 2021. Nonstationary bubble shape determination in electrical impedance tomography combining Gauss–Newton optimization with particle filter. *Measurement* (186), 110216. <https://doi.org/10.1016/j.measurement.2021.110216>.
- Dumitrescu, D.T., 1943. Strömung an einer Luftblase im senkrechten Rohr. *Z. Angew. Math. Mech.* 23, 139–149. <https://doi.org/10.1002/zamm.19430230303>.
- Fabre, J., Figueroa-Espinoza, B., 2014. Taylor bubble rising in a vertical pipe against laminar or turbulent downward flow: symmetric to asymmetric shape transition. *J. Fluid Mech.* 755, 485–502. <https://doi.org/10.1017/jfm.2014.429>.
- Fershtman, A., Babin, V., Barnea, D., Shemer, L., 2017. On shapes and motion of an elongated bubble in downward liquid pipe flow. *Phys. Fluids* 29, 112103. <https://doi.org/10.1063/1.4996444>.
- Fershtman, A., Barnea, D., Shemer, L., 2021. Wave identification in upward annular flow – a focus on ripple characterization. *Int. J. Multiphase Flow* 137, 103560. <https://doi.org/10.1016/j.ijmultiphaseflow.2021.103560>.
- Fershtman, A., Robers, L., Prasser, H.-M., Barnea, D., Shemer, L., 2020. Interfacial structure of upward gas-liquid annular flow in inclined pipes. *Int. J. Multiphase Flow* 132, 103437. <https://doi.org/10.1016/j.ijmultiphaseflow.2020.103437>.
- Figueroa-Espinoza, B., Fabre, J., 2011. Taylor bubble moving in a flowing liquid in vertical channel: transition from symmetric to asymmetric shape. *J. Fluid Mech.* 679, 432–454. <https://doi.org/10.1017/jfm.2011.159>.
- Frederix, E.M.A., Komen, E.M.J., Tiselj, I., Mikuz, B., 2020. LES of turbulent co-current Taylor bubble flow. *Flow Turbulence Combust.* 105, 471–495. <https://doi.org/10.1007/s10494-020-00118-0>.
- Fukagata, K., Kasagi, N., 2002. Highly energy-conservative finite difference method for the cylindrical coordinate system. *J. Comput. Phys.* 181, 478–498.
- Grishchenko, D., 2011. KROTOS Image Analysis for Water-Corium Interactions (KIWI). OECD SERENA project report DEN/DTN/STRI/LMA/NT/2011/009/0, CEA, France.
- Gutiérrez, E., Balcázar, N., Bartrons, E., Rigola, J., 2017. Numerical study of Taylor bubbles rising in a stagnant liquid using a level-set/moving-mesh method. *Chem. Eng. Sci.* 164, 158–177. <https://doi.org/10.1016/j.ces.2017.02.018>.
- Kemper, P., Küstermann, E., Dreher, W., Helmers, T., Mießner, U., Besser, B., Thöming, J., 2021. Magnetic resonance imaging for non-invasive study of hydrodynamics inside gas-liquid Taylor flows. *Chem. Eng. Technol.* 44, 465–476. <https://doi.org/10.1002/ceat.202000509>.
- Kockx, J.P., Nieuwstadt, F.T.M., Oliemans, R.V.A., Delfos, R., 2005. Gas entrainment by a liquid film falling around a stationary Taylor bubble in a vertical tube. *Int. J. Multiphase Flow* 31, 1–24. <https://doi.org/10.1016/j.ijmultiphaseflow.2004.08.005>.
- Liberzon, D., Shemer, L., Barnea, D., 2006. Upward-propagating capillary waves on the surface of short Taylor bubbles. *Phys. Fluids* 18, 048103. <https://doi.org/10.1063/1.2192781>.
- Lin, R., Wang, K., Liu, L., Zhang, Y., Dong, S., 2020. Study on the characteristics of interfacial waves in annular flow by image analysis. *Chem. Eng. Sci.* 212, 115336. <https://doi.org/10.1016/j.ces.2019.115336>.
- Liu, X., Ozbayoglu, E.M., Upchurch, E.R., Baldino, S., 2023. Computational fluid dynamics simulations of Taylor bubbles rising in vertical and inclined concentric annuli. *Int. J. Multiphase Flow* 159, 104333. <https://doi.org/10.1016/j.ijmultiphaseflow.2022.104333>.
- Lizarraga-Garcia, E., Buongiorno, J., Al-Safran, E., 2021. Computational fluid dynamics (CFD) simulations of Taylor bubbles in vertical and inclined pipes with upward and downward liquid flow. *SPE J.* 26, 3832–3847. <https://doi.org/10.2118/205373-PA>.
- Lou, W., Wang, Z., Guo, B., Pan, S., Liu, Y., Sun, B., 2022. Numerical analysis of velocity field and energy transformation, and prediction model for Taylor bubbles in annular slug flow of static power law fluid. *Chem. Eng. Sci.* 250, 117396. <https://doi.org/10.1016/j.ces.2021.117396>.
- Lu, X., Prosperetti, A., 2006. Axial stability of Taylor bubbles. *J. Fluid Mech.* 568, 173–192.
- Mao, Z.S., Dukler, A.E., 1991. The motion of Taylor bubbles in vertical tubes—II. Experimental data and simulations for laminar and turbulent flow. *Chem. Eng. Sci.* 46, 2055–2064. [https://doi.org/10.1016/0009-2509\(91\)80164-T](https://doi.org/10.1016/0009-2509(91)80164-T).
- Martin, C.S., 1976. Vertically downward two-phase slug flow. *ASME J. Fluids Eng.* 98 (4), 715–722. Dec 1976.
- Mikuz, B., Frederix, E.M.A., Komen, E.M.J., Tiselj, I., 2020. Taylor bubble behaviour in turbulent flow regime. In: *Proceedings of the Conference Computational Fluid Dynamics for Nuclear Reactor Safety (CFD4NRS-8)* 12.
- Mikuz, B., Kamnikar, J., Prošek, J., Tiselj, I., 2019. Experimental observation of Taylor bubble disintegration in turbulent flow. In: *Proceedings of the 28th International Conference Nuclear Energy for New Europe* 9.
- Mitchell, T., Leonardi, C., 2020. On the rise characteristics of Taylor bubbles in annular piping. *Int. J. Multiphase Flow* 130, 103376. <https://doi.org/10.1016/j.ijmultiphaseflow.2020.103376>.
- Moody, L.F., 1944. Friction factors for pipe flow. *Trans. ASME* 66 (8), 671–684.
- Moreira, T.A., Morse, R.W., Dressler, K.M., Ribatski, G., Berson, A., 2020. Liquid-film thickness and disturbance-wave characterization in a vertical, upward, two-phase annular flow of saturated R245fa inside a rectangular channel. *Int. J. Multiphase Flow* 132, 103412. <https://doi.org/10.1016/j.ijmultiphaseflow.2020.103412>.
- Morgado, A.O., Miranda, J.M., Araújo, J.D.P., Campos, J.B.L.M., 2016. Review on vertical gas-liquid slug flow. *Int. J. Multiphase Flow* 85, 348–368. <https://doi.org/10.1016/j.ijmultiphaseflow.2016.07.002>.
- Nicklin, D.J., Wilkes, J.O., Davidson, J.F., 1962. Two-phase flow in vertical tubes. *Trans. Inst. Chem. Eng.* 40, 61–68.
- Pan, L., He, H., Ju, P., Hibiki, T., Ishii, M., 2015. Experimental study and modeling of disturbance wave height of vertical annular flow. *Int. J. Heat Mass Transfer* 89, 165–175. <https://doi.org/10.1016/j.jheatmasstransfer.2015.05.073>.
- Pearce, D.L., 1979. Film waves in horizontal annular flow: space-time correlator experiments. *CERL Note RD/L/N111/79*.
- Pinto, A.M.F.R., Coelho Pinheiro, M.N., Nogueira, S., Ferreira, V.D., Campos, J.B.L.M., 2005. Experimental study on the transition in the velocity of individual Taylor bubbles in vertical upward co-current liquid flow. *Chem. Eng. Res. Des.* 83, 1103–1110. <https://doi.org/10.1205/cherd.03238>.
- Polonsky, S., Barnea, D., Shemer, L., 1999. Averaged and time-dependent characteristics of the motion of an elongated bubble in a vertical pipe. *Int. J. Multiphase Flow* 25, 795–812. [https://doi.org/10.1016/S0301-9322\(98\)00066-4](https://doi.org/10.1016/S0301-9322(98)00066-4) pg.
- Polonsky, S., Shemer, L., Barnea, D., 1999. The relation between the Taylor bubble motion and the velocity field ahead of it. *Int. J. Multiphase Flow* 25, 957–975. [https://doi.org/10.1016/S0301-9322\(99\)00037-3](https://doi.org/10.1016/S0301-9322(99)00037-3) pg.
- Porombka, P., Boden, S., Lucas, D., et al., 2021. Horizontal annular flow through orifice studied by X-ray microtomography. *Exp. Fluids* 62, 5. <https://doi.org/10.1007/s00348-020-03091-6>.
- Press, W.H., Teukolsky, S.A., Vetterling, W.T., Flannery, B.P., 2007. *Numerical Recipes 3rd Edition: The Art of Scientific Computing 3rd Edition*. Cambridge Press, 2007.
- Rivera, Y., Berna, C., Muñoz-Cobo, J.L., Escrivá, A., Córdova, Y., 2022. Experiments in free falling and downward cocurrent annular flows – Characterization of liquid films and interfacial waves. *Nucl. Eng. Des.* 392, 111769. <https://doi.org/10.1016/j.nucengdes.2022.111769>. ISSN 0029-5493.
- Rohilla, L., Kumar Das, A.K., 2020. Modeling interaction between a Taylor bubble and small bubble in a rectangular column. *Phys. Fluids* 32, 112106. <https://doi.org/10.1063/5.0024728>.
- Schubring, D., Shedd, T.A., Hurlburt, E.T., 2010. Studying disturbance waves in vertical annular flow with high-speed video. *Int. J. Multiphase Flow* 36 (5), 385–396. <https://doi.org/10.1016/j.ijmultiphaseflow.2010.01.003>.
- Shemer, L., Gulitski, A., Barnea, D., 2005. Experiments on the turbulent structure and the void fraction distribution in the Taylor bubble wake. *Mult. Sci. Technol.* 17, 103–122. <https://doi.org/10.1615/MultScienTechn.v17.i1.2.60>.
- Shemer, L., Gulitski, A., Barnea, D., 2007. On the turbulent structure in the wake of Taylor bubbles rising in vertical pipes. *Phys. Fluids* 19, 035108. <https://doi.org/10.1063/1.2711478>.
- Taha, T., Cui, Z.F., 2006. CFD modelling of slug flow in vertical tubes. *Chem. Eng. Sci.* 61 (2), 676–687. <https://doi.org/10.1016/j.ces.2005.07.022>.
- Wallis, G.B., 1969. *One-Dimensional Two-Phase Flow*. McGraw Hill.
- Wang, C., Zhao, N., Peng, Y., Sun, H., Fang, L., 2018. Interfacial wave velocity of vertical gas-liquid annular flow at different system pressures. *Exp. Therm Fluid Sci.* 92, 20–32. <https://doi.org/10.1016/j.expthermflusci.2017.09.007>.

Wang, X., Zhang, J., Chen, Y., Kuai, Z., 2023. Numerical study of rising Taylor bubbles driven by buoyancy and additional pressure. *Int. J. Multiphase Flow* 159, 104309. <https://doi.org/10.1016/j.ijmultiphaseflow.2022.104309>.

Yoshida, K., Fujiwara, K., Nakamura, Y., Kaneko, A., Abe, Y., 2022. Experimental study of interfacial area of bubble plume based on bubble tracking by wire-mesh sensor.

Nucl. Eng. Des. 388 <https://doi.org/10.1016/j.nucengdes.2021.111645> art. no. 111645.

Zhou, G., Prosperetti, A., 2019. Violent expansion of a rising Taylor bubble. *Phys. Rev. E: Stat. Phys., Plasmas, Fluids, Relat. Interdiscip. Top.* 4, 073903 <https://doi.org/10.1103/PhysRevFluids.4.073903>.